ESCUELA SUPERIOR DE INGENIERÍA

GRADO EN INGENIERÍA AEROESPACIAL

NUMERICAL ANALYSIS OF A PWC PROPULSION SYSTEM WITH OPENFOAM®

AUTOR: ÁLVARO GARCÍA PEÑA

Cádiz, julio 2017

ESCUELA SUPERIOR DE INGENIERÍA

GRADO EN INGENIERÍA AEROESPACIAL

NUMERICAL ANALYSIS OF A PWC PROPULSION SYSTEM WITH OPENFOAM®

DIRECTOR: ANTONIO MARTÍN ALCÁNTARA
CODIRECTOR: ANTONIO JUAN GÁMEZ LÓPEZ
AUTOR: ÁLVARO GARCÍA PEÑA

Cádiz, julio 2017

Abstract

The personal watercraft (PWC) concept was originated in the 1960s. Since then, PWCs have been developed to provide more powerful and efficient vehicles. The key of these improvements lies on their propulsion system, which roughly consists of a dynamic (impeller) and a static (stator) part in a confined tube. Therefore, the overall aim of this project is to develop a numerical study of a PWC jet-pump based on the existing configuration for a *Bombardier xp 951 99*, considering not only the impeller and the stator, but the whole propulsion system in order to approach a solution to the real problem. More specifically, this study is aimed to achieve a description of the flow behavior, analyzing the results for several force coefficients such as the thrust C_t and momentum coefficient C_m at different operating conditions. On the other hand, CAESES is used to model the domain under consideration. Numerical simulations are performed by means of OpenFOAm®, whose built-in utility `snappyHexMesh` is used to generate the computational grid. Turbulent, incompressible, 3D simulations based on the Reynolds Averaged Navier-Stokes (RANS) approach are performed. The sliding-mesh technique Arbitrary Mesh Interface (AMI) is considered to achieve the sliding grid that will allow the impeller to rotate. For the entire bulk of the stack of simulations, the incompressible solver `pimpleDyMFoam` is used.

Contents

List of Figures

List of Tables

NOMENCLATURE

Abbreviations

AMI Arbitrary Mesh Interface

BSL Baseline

CFD Computational Fluid Dynamics

DES Detached Eddy Simulation

DNS Direct Numerical Simulation

FVM Finite Volume Method

GCI Grid Convergence Index

IVR Inlet Velocity Ratio

JVR Jet Velocity Ratio

LES Large Eddy Simulation

N-S Navier Stokes

PWC Personal Watercraft

RANS Reynolds Averaged Navier-Stokes

RPM Revolutions per Minute

SST Shear Stress Transport

Symbols

α Inlet flow angle seen by the impeller

Δ Increment ratio of venturi outlet diameter

ϵ Rate of dissipation of turbulence kinetic energy

$\boldsymbol{\tau}$ Stress tensor

$\boldsymbol{\tau}^R$ Reynolds stress tensor

$\mathbf{I}$ Identity matrix

$\mathbf{v}$ Velocity vector

$\mathbf{x}$ Position vector

μ Dynamic viscosity

μ Kinematic viscosity

μ_t Turbulent viscosity

∇ Nabla operator

Ω	Normalized impeller angular velocity
∂	Partial derivative
ϕ	Trailing edge pitch angle
ρ	Density
τ	Normalized time
C_m	Momentum or torque coefficient
C_p	Pressure coefficient
C_t	Thrust coefficient
D	Impeller diameter
D_0	Venturi outlet diameter
f_b	Body forces
h	Grid Spacing
k	Turbulent kinetic energy
p	Static pressure
p_0	Reference pressure
Q	Volumetric flow rate
Q^*	Normalized volumetric flow rate
T	Increment of time
V	Ship velocity
V_p	Averaged axial inflow velocity at the pump section
t	Time

1 Introduction

The usage of Computational Fluid Dynamics (CFD) tools has become crucial to the development of a wide range of modern technologies. Essentially, the overall aim of such applications consists of approaching the Navier-Stokes (N-S) equations, which have been used in the field of CFD by researchers for more than a hundred years. Specially, the use of OpenFOAM® for CFD applications is widely spread across industrial and academic environments, whose principal advantage lies on its General Public License, leading to huge cost reductions. Especially, OpenFOAM® has experimented an important growth for the last years, increasing the number of solvers and applications since its first releases. In this context, CFD tools might come in very useful on a field where conventional blade theory cannot provide an accurate prediction of the flow behavior and overall performance of jet-pumps, although most of researches on water-jet propulsion have been carried out only by experiments (see Kelth et al., 1994; Allison, 1993). Moreover, testing procedures may be very expensive and time-consuming, unlike CFD tools, which makes it possible to accurately predict detailed flow fields in water-jet pumps.

Particularly, so many studies, such as those by Bulten (2006), Peixin and Mehrdad (1999) or Park et al. (2005a), emphasize the importance of understanding the flow behavior within the intake housing or duct when evaluating the overall performance of the system. A numerical and experimental analysis was also performed by Park et al. (2005b) in order to provide a detailed understanding of the intake duct of a water-jet at different operating conditions.

Finally, jet-pumps are manufactured on the basis of maximizing efficiency, causing the system to work outside of its optimal operating range. It is commonly known that the relationship between the impeller and pump exit nozzle diameter is critical to the performance of the watercraft. So, in the present work, the behavior for the current jet-pump is changed by means of variations on the pump exit for the same impeller design, attempting to obtain the maximum thrust generation regardless of the torque or momentum coefficient required to achieve this purpose. A similar statement can be made for the trailing edge pitch angle.

1.1 Objectives of the project

The main purpose of this project is to develop a numerical study on the performance of a Personal Watercraft (PWC) propulsion system, achieving a better understanding of the flow behavior on this evolutionary field. For this purpose, turbulent, incompressible, 3D simulations with a dynamic mesh were performed by using OpenFOAM®. The geometric domain under consideration is based on the existing configuration for a *Bombardier xp 951 99*. The modeling of the whole jet-pump, also known as jet-drive, will be carried out by means of CAESES, a software platform for the design of complex 3D surfaces. Realistic results are expected from such a detailed representation of the propulsion system.

The flow through a jet drive is known to be a high-Re problem, so Reynolds Averaged Navier-Stokes (RANS) approach were used in order to tackle turbulence effects. On the other hand, the Arbitrary Mesh Interface (AMI) technique available in OpenFOAM® is used to model the rotating motion of the impeller. In such manner, macroscopic effects are studied, analyzing parameters such as the thrust generation, and illustrating with some examples some possible design improvements. Finally, some conclusions resulting from

the numerical analysis and future works are presented.

1.2 Structure of the work

To completely understand the present work and its application, some basic and important factors about jet-pumps and PWC impellers are introduced in this section. Then, a theoretical background is presented starting with the Finite Volume Method (FVM) in OpenFOAM® along with a brief description of the general governing equations (see section 2). An overview about how turbulences are treated and several approaches to turbulence modeling are included in section 3, where RANS model are presented and two equations models are treated (section 3.2 and 3.4 respectively). At this point, a definition of the problem under consideration is carried out, the parameters under study as well as the general assumptions performed so as to tackle the real problem (see section 4.2).

On the other hand, a geometric representation of the propulsion system for a *Bombardier xp 951 99* PWC in CAESES platform is carried out (see section 4.3 and Appendix B for a better understanding). Secondly, the respective meshing procedure by `snappyHexMesh` can be analyzed within section 5.1, whose validation procedure is exhibited in Appendix E. Information about boundary conditions (BC) as well as the numerical schemes can be found in section 4.4 and 5.2 respectively. Appendix A shows a detailed review of the OpenFOAM® case directory and how BC have been implemented. Finally, results are discussed and some conclusions are extracted from the CFD analysis (section 6).

1.3 Jet-pump and PWC impeller fundamentals

First of all, PWC propulsion systems are composed of axial-flow jet-pumps, in relation to their shaft axis. Within the main parts included within this kind of water-jet system, also known as jet-drive systems, a ducted propeller or impeller can be found, whose torque is transmitted by the drive shaft, connected directly to the engine output on the opposite end. A intake housing, commonly known as gullet, surrounds the transmission and impeller. The housing or stator can be found successively to the impeller, which is made of vanes that remain still. Finally, a rear venturi and steering nozzle can be observed. A typical representation of a water-jet based propulsion system is shown in Figure 1.1.

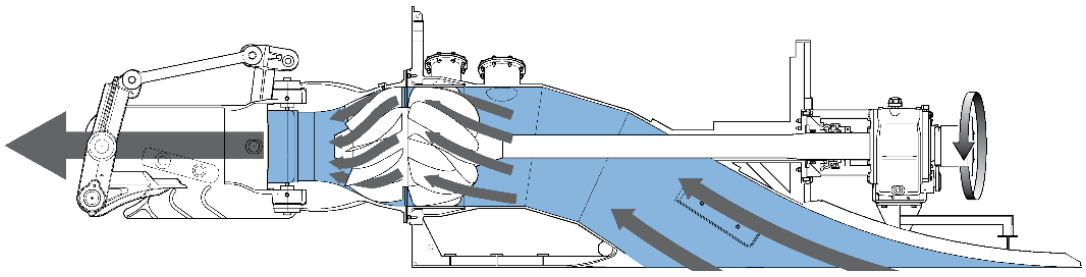

Figure 1.1: Typical axial jet-pump. Image from WARTSILA (2017).

Particularly, the cutting plane for a *Sea-Doo xp 951 99* jet-pump, under consideration in the present work, is shown in figure 1.2.

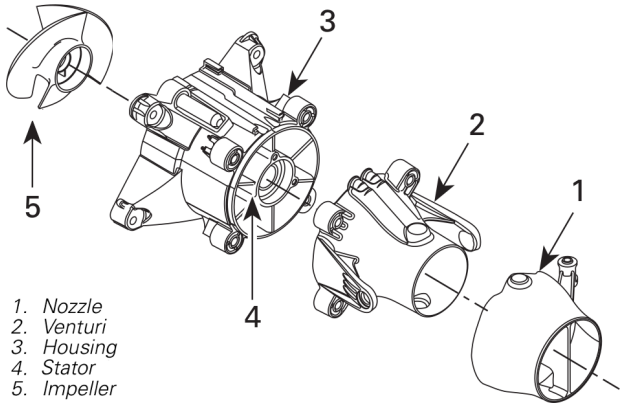

Figure 1.2: Sea-Doo xp 951 99 Jet-Pump Cutting Plane. Image from Bombardier (1999).

where the drive shaft and the gullet have been omitted.

Thrust Generation

When analyzing impellers, or ducted propellers, it is also necessary to have under considerations the shroud or housing itself. It forces water backwards, producing greater efficiency than the impeller by itself, which is highly inefficient since it will only scatter water. In the same way as any other propeller operating either on air or water, impellers work on the principal of pressure gradients. As blades rotate, water is pushed backwards and outwards. Positive pressure on every blade face and negative pressure on the blade back results in a pressure differential between both sides of each blade, producing a pushing force. This phenomena will also create a spiraling effect, in which generated water vortices must pass through stators or straightening vanes in order to straighten or right its trajectory when leaving the trailing edge of the blades. Vanes also increase its velocity by a "catapulting" effect on water.

Finally, water pases through the so called venturi (see Part 2 in Figure 1.2) in order to further enhance velocity before leaving the pump and so generating thrust. Torque is transfered to the impeller through the drive shaft, which is connected to the engine on the opposite side. The gullet is the area forward of the impeller, also known as intake housing or duct, which channels water toward the impeller via vacuum.

Impeller efficiency is strongly related to other design parameters that make up the jet-pump, e.g gullet area, stator blade area, angle of vanes, venturi rate of compression and exiting area, pump placement within the hull, and so on.

Additional technical information can be found in the working principles or axial pumps section of any book about turbomachines and fluid mechanics, e.g., (Dixon and Hall, 1998) or (Dick, 2015).

PWC Impellers

When an impeller is designed by manufactures, they are intended to apply to a wide range of PWC pumps. Additionally, the main goal is to reach the best overall performance and

efficiency possible to accommodate a wide variety of users, providing with both bottom-end and top speed without having to compromise. However, every craft is a little different, every riders' performance desires vary from one to another. Many variables and factors related to riding conditions such as the weight can make the performance fluctuate. So, for example, one may have a great overall performing impeller but without squeezing every bit of top speed or bottom end out of it. On the other hand, one may also want to add more horsepower to your engine and you will get to a point when that great overall performing impeller is not aggressive enough to match the new power. In this way, horsepower (torque) and RPM will also be determining when choosing a particular impeller.

Many design parameters are included when designing a PWC impeller, such as the pitch, rake, the sweep or skew and so on. These parameters are modified by manufactures in order to satisfy the different riding conditions, which are ruled by previously explained factors such as weight, horsepower, RPM, etc. Some of the most influential parameters when designing a PWC impeller are presented below.

- Material: The use of stainless steel decreases the necessary amount of the previously used aluminum needed, maintaining the strength. This also minimize the hub diameter, increasing the blade area available which water could pass through and so increasing thrust.

- Over-lapping blades: The use of over-lapping blades give an increased blade area that leads to greater acceleration of water, bringing more water up into the gullet and enhancing the thrust.

- Variable Hub Area: As water enters the leading edge of the blade and it its accelerated, the increasing size of the hub works with centrifugal force to push water toward the outside edge of the blade. This collective action increases velocity of the water whose trajectory is then straighten backwards by the shroud.

- Pitch: This is a commonly known statement, "larger pitch can grab too much water, over-load the engine and reduce acceleration, however, it will increase the top speed. On the contrary, smaller pitch gives greater acceleration, but reduces top speed". Nevertheless, by combining smaller pitch at the leading edge and transitioning to a larger pitch at the trailing edge, the most use of both facts can be made. Besides, a less aggressive pitch at the leading edge reduces laminar separation, which hence will minimize cavitation. In a progressive pitch impeller examined from the side, the pitch angle is constant where it is attached to the hub, but the outer edges of the blade are not.

- Kicks: The closest area to the trailing edge with increasing pitch "catapults" water and increases velocity.

- Sweeps: In comparison to a perpendicular to the hub leading edge that "chops" through water, a swept leading edge that slices through water will reduce cavitation. It also can be used in order to gain some more blade area.

In case of the weight, some watercraft are designed to carry from 1 up to 4 people, which involves a varying carried weight that can fluctuate to more than 200kg, or even more when pulling a water skier. Although watercrafts are equipped with a good all-around performing impeller, heavy loads make it harder for the engine to respond as quickly and

additional low-end thrust would be beneficial. This extra bottom-end power can be obtained by adjusting the impeller. So higher performance with an overloaded watercraft can be accomplished by reducing the pitch of the impeller. On the contrary, when carrying substantially less weight extra performance can be gained by raising the pitch of the impeller and so obtaining higher speed values.

On the other hand, in case of dealing with horsepower, a common assumption is "the more horsepower you have, the higher pitch impeller needed ". Nevertheless, that is not necessarily the case, changes in the pitch values can be deceiving since many factors and critical things are to be considered when an impeller is designed, engine characteristics (RPM available), a large number of impeller design parameters, riding conditions (hull weight) and so on. So making the right choice for a certain situation may be quite complicated.

Since there is no specific documentation with regard to PWC impellers, further information about this topic can be found from official dealers.

2 OpenFOAM® and the Finite Volume Method

2.1 OpenFOAM®

OpenFOAM® is the leading open source software for CFD. Created in 1989, it has continued to be developed with new versions each year. Its working principle lies on the Finite Volume Method (FVM), which discretizes the governing equations by using a methodology on unstructured polyhedral grids and centering the flow field quantities on the control volume centroids, allowing a large variety of available solution schemes to solve them.

In comparison to the finite difference or finite element method, there are some properties which make the FVM the preferred method in CFD, which are introduced in section 2.3.

2.2 Governing equations

The governing equations of the fluid flow are generally known as the Navier-Stokes equations. The origin and explanation of the physical laws, conservation principles and other related transport phenomena from which these equations derive is beyond the scope of this work and it is not absolutely necessary for the reader to understand the subsequent results. Additional information about this section can be found from Moukalled et al. (2015) or Hauke (2008).

Continuity Equation

Based on the principle of conservation of mass, the form of the continuity equation for an incompressible fluid is given by:

$$\nabla \cdot \mathbf{v} = 0. \tag{2.1}$$

Continuity equation states that net flow in and out across any control volume will be zero. Note that the approximation of incompressibility has been made $D\rho/Dt = 0$, which does not imply that ρ is the same everywhere, but that each fluid element will keep its original density as it moves. In practice, density differences are commonly encountered in water due to variation in salt concentration, but it will be supposed constant in this study.

Momentum Equation

The momentum equation stems from the principle of conservation of linear momentum. Reconsidering the assumptions previously made, for a Newtonian, incompressible fluid, the momentum equation reduces to the following expression

$$\frac{\partial}{\partial t}[\rho \mathbf{v}] + \nabla \cdot [\rho \mathbf{v}\mathbf{v}] = -\nabla p + \mu \nabla^2 \mathbf{v} + \mathbf{f}_b, \tag{2.2}$$

where $\rho\mathbf{v}\mathbf{v}$ is a dyadic product, $\mathbf{f}_b$ represents body forces. Gravitational force is the only body force and it acts along the negative z-axis.

General Conservation Equation

The governing equations described above are written in terms of specific quantities. The momentum equation, for instance, expresses the principle of conservation of linear momentum in terms of the velocity. However, the same type of conservation equation may

be applied to any intensive property ϕ that need to be calculated. So, a general equation that can represent any of the conservation equations can be written as follows

$$\underbrace{\frac{\partial}{\partial t}(\rho\phi)}_{unsteady\,term} + \underbrace{\nabla\cdot(\rho\mathbf{v}\phi)}_{convection\,term} = \underbrace{\nabla\cdot(\Gamma^{\phi}\nabla\phi)}_{diffusion\,term} + \underbrace{Q^{\phi}}_{source\,term} \quad . \tag{2.3}$$

For an arbitrary fixed control volume, unsteady and convection term express the change of ϕ over time within the material volume, where $\rho\mathbf{v}\phi$ represents the transport of ϕ by the flow field. The diffusion term, represents the surface flux of ϕ over time, which in this case, the physical phenomena that causes this flux in or out of ϕ is the diffusion physical phenomena, produced by molecular collision, where Γ^{ϕ} is the diffusion coefficient of ϕ. Finally, the source term Q^{ϕ} express the generation or destruction of ϕ within the control volume.

2.3 Finite Volume Method

The partial differential equations that govern the flow field, which are introduced in the previous section, need to be replaced by a system of algebraic equations that can be solved. In such manner, the FVM is a numerical technique which transforms/discretizes the set of partial differential equations, representing conservation laws over differential volumes, into a system of discrete algebraic equations over finite volumes by integrating them over each discrete element.

Main properties that make FVM preferable for CFD applications are introduced below.

- FVM is strictly conservative.
- It can be formulated on unstructured polygonal meshes.
- Boundary conditions implemented in a non-invasive manner quite easily.
- The method is applicable to both steady and transient calculations.

The first characteristic refers to the fact that the flux entering a given volume is identical to that leaving the adjacent volume. Some of the terms in the conservation equation are turned into face fluxes and evaluated at the finite volume faces. So basic quantities, such as the mass and momentum will therefore be conserved. The second feature is particularly useful in meshing complex geometries as explained subsequently in section 5.1. The third makes reference to the fact that unknown variables are evaluated at the centroids of the volume elements, not at their boundary faces, making more efficient the implementation of boundary conditions.

So, in similar fashion to other numerical methods, the discretization process can be divided into two steps. The first is the discretization of the geometric domain. Then, the system of algebraic equations is solved in order to compute the values of the dependent variable for each discrete element.

Discretization of the domain produces a computational grid which includes the positions of points where the governing equations are subsequently solved. These points, known as cells or control volumes, determine the positions where the solution is sought. The time interval is also split into a finite number of time-steps for transient simulations. So the process can be split into discretization of time and space.

Figure 2.1 shows a general polyhedron representing a typical control volume (CV), where P is located at its centroid and N at the neighbor cell center. The flat faces in which the CV is bounded, denoted by f, represent either the same for neighboring cells, known as internal faces (located between two control volumes), or the boundary faces, which correspond to the boundaries of the domain. On the other hand, the face area normal vector **S** is generated for each face and stores the area of the face.

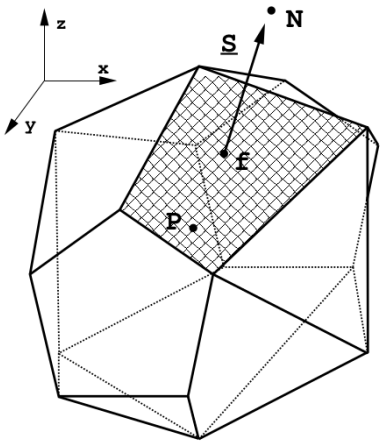

Figure 2.1: Cells in domain discretization by FVM. Image from Jasak (1996).

Since the FVM encompasses a wide range of conceptual and mathematical approaches beyond the scope of this analysis, see thesis by Jasak (1996) or specific FVM documentation, e.g. from Moukalled et al. (2015); Ferziger and Perić (2002), for a more detailed review of this method.

3 Turbulence modeling

Considering the fact that turbulence modeling is a extremely large topic, the main goal of this chapter will keep the details of the mathematical modeling to a minimum, developing a qualitative standpoint and introducing some of the most popular turbulence models.

First of all, its important to notice that laminar flows are stable while turbulent flows are chaotic, rapid mixing, time-dependent and involve three-dimensional vorticity fluctuations. Turbulence arises as an instability of laminar flows under certain conditions at a particular critical Reynolds number. The most accepted theory of turbulence is based on the "energy cascade" concept (see Moukalled et al., 2015), which states that turbulence is composed of eddies whose energy depends on its dimension. The larger eddies transfer their energy to smaller newly formed eddies in a chain process when the first breaks up. When the smallest possible eddies are reached, they dissipate the turbulent kinetic energy as heat, since the molecular viscosity is very effective at that scale.

3.1 Turbulence modeling methods

In order to resolve the mentioned turbulent and chaotic flow, a numerical solution deriving directly from the N-S equations will require the use of a extremely fine mesh and a very small time step. This approach to resolve the flow field is known as Direct Numerical Simulation (DNS) and will demand prohibitive computational costs. Thus, statistical analysis, which are computationally less intensive than the DNS, are used to simplify the resolution of turbulent flows. In total, there are generally four different approaches to model turbulence (see Figure 3.1), which can be arranged according to their complexity and so their required computational effort (see Maric et al., 2014).

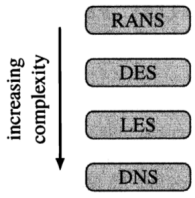

Figure 3.1: Complexity scheme of several turbulence modeling methods. Image from Maric et al. (2014).

The most basic category of turbulence models are the Reynolds Averaged Navier-Stokes (RANS) models, which are the most popular approach to tackling industrial turbulent flow problems. All the models of this group work on the temporal fluctuation of the mean velocity. The turbulent fluctuations (eddies) are not resolved geometrically, but modeled, so they can work on comparatively coarse grids and so computational efforts are relatively lower. For this reason, only RANS models are covered in this work. Examples for RANS models are the k-ϵ model, the k-ω model and the k-ω-SST model.

Large Eddy Simulation (LES) models differ from the first one so that large scale eddies are resolved geometrically by the computational grid and only the smallest one are modeled. Thus, LES approaches need a significantly finer mesh.

The idea of Detached Eddy Simulation (DES) is a hybrid strategy for the computation of massively separated flows. It is based on a common RANS model which switches to

"LES-mode" in regions away from the wall and *vice versa*.

DNS methods solve the N-S equations for all flow scales, as previously mentioned. It is the simplest as regard to implementation, but the required computational efforts are extremely high. Thus, DES, LES and DNS are not covered in this work.

3.2 Reynolds Averaged Navier-Stokes (RANS)

RANS equations are based on the Reynolds Averaging procedure, which consist of decomposing any of the flow variables involved into a mean value and a fluctuating component (see eq. 3.1 and Figure 3.2). Then, even though the name refers to the N-S equations, substitution is applied to all governing equations.

$$\phi(\mathbf{x},t) = \overline{\phi}(\mathbf{x},t) + \phi'(\mathbf{x},t), \tag{3.1}$$

where $\phi(\mathbf{x},t)$ represents any of the flow variables at time t and position $\mathbf{x}$, such as $\mathbf{v}$, p,ρ and so on. $\overline{\phi}$ symbolize the mean value component and ϕ' represents the fluctuating component.

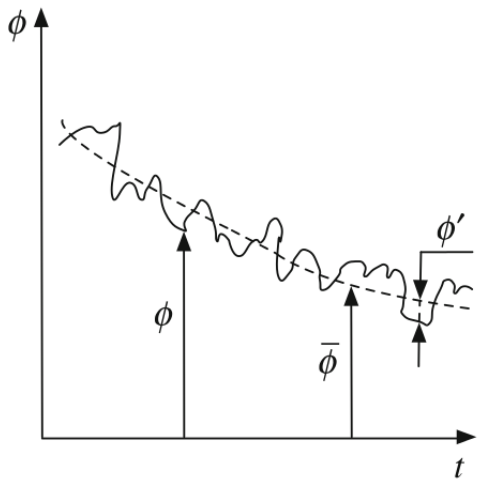

Figure 3.2: Mean value and fluctuating component in Reynolds Averaging procedure. Image from Moukalled et al. (2015).

The mean value $\overline{\phi}$ can be computed by using any of the three Reynolds averaging techniques; time averaging, spatial averaging and ensemble averaging. However, time averaging is the most widely used. The Averaged terms will refer to this averaging technique from now on, so that $\overline{\phi}$ can be expressed as follows

$$\overline{\phi}(\mathbf{x},t) = \lim_{T\to\infty} \frac{1}{T} \int_t^{t+T} \phi(\mathbf{x},t)dt, \tag{3.2}$$

where Considering the assumption of Newtonian, incompressible flow and taking the time average, the RANS equations, derives from the N-S equations, can be written as:

$$\nabla \cdot [\rho\overline{\mathbf{v}}] = 0, \tag{3.3}$$

$$\frac{\partial}{\partial t}[\rho\overline{\mathbf{v}}] + \nabla\cdot[\rho\overline{\mathbf{v}}\overline{\mathbf{v}}] = -\nabla\overline{p} + [\nabla\cdot(\overline{\tau} + \boldsymbol{\tau}^R] + \mathbf{f}_b, \tag{3.4}$$

where $\boldsymbol{\tau}^R = -\rho\overline{\mathbf{v}'\mathbf{v}'}$ is known as the Reynolds stress tensor and its calculation is denoted by turbulence modeling. Nevertheless, additional equations are required. So, according to the Boussinesq hypothesis for incompressible flows, the Reynolds stress reduces to

$$\boldsymbol{\tau}^R = \mu_t\{\nabla\overline{\mathbf{v}} + (\nabla\overline{\mathbf{v}})^T\} - \frac{2}{3}\rho k\mathbf{I}, \tag{3.5}$$

where μ_t is the turbulent eddy viscosity, which is now flow,not fluid, dependent, and k is the turbulent kinetic energy defined as

$$k = \frac{1}{2}\overline{\mathbf{v}' \cdot \mathbf{v}'}. \tag{3.6}$$

The problem now is transformed into computing the turbulent kinetic energy and turbulent viscosity.

3.3 Turbulence models

In order to express the turbulent viscosity, μ_t, in terms of the turbulent kinetic energy, k, several turbulence models has been developed, but none of them is applicable to all flow conditions. These models are grouped into four main categories depending on the nature and number of equations that are used to compute μ_t.

- Algebraic Models
- One-Equation Models
- Two-Equation Models
- Second-Order Closure Models

Where the last is the most computationally expensive. The two-equation models are the most widespread in terms of usage due to the delivery of accurate enough predictions, in which the $k-\epsilon$ model is the most popular, followed by the $k-\omega$ model. So the attention will be focused on the two-equation models.

The present section will be focused on a descriptive standpoint. See Moukalled et al. (2015); Ferziger and Perić (2002) or Versteeg and Malalasekera (1995) for a detailed review of this models.

3.4 Two-equation turbulence models

Standard $k-\epsilon$ model

The $k-\epsilon$ model approximates the turbulent viscosity as

$$\mu_t = \rho C_\mu \frac{k^2}{\epsilon}, \tag{3.7}$$

where ϵ is the rate of dissipation of turbulent kinetic energy per unit mass and C_μ is a constant.
The standard $k-\epsilon$ model is derived assuming the flow to be fully turbulent and the effects of molecular viscosity to be negligible. Due to this fact, the family of $k-\epsilon$ models are well behaved for free-shear flows while are likely to fail predicting flows with adverse pressure gradient. Therefore, this is a high Reynolds number turbulent model valid only for fully turbulent free shear flows and so it cannot be integrated all the way to the wall. For this purpose, a low Reynolds number turbulent model would be required. However, several low Reynolds number $k-\epsilon$ models have been proposed over the years based on the usage of additional functions.

$k-\omega$ model

In this case, the equation 3.7 is replaced by an equation for ω,

$$\omega = \frac{\epsilon}{C_\mu k}, \tag{3.8}$$

which is the rate at which turbulent kinetic energy is converted into internal thermal energy per unit volume and time, known as the specific turbulence dissipation. The $k-\omega$ model can also be used as a high Reynolds number turbulent model, but also it has low Reynolds number formulation. Generally, the $k-\omega$ is easier to integrate (more robust) and it can be integrated all the way to the wall without the need to employ additional functions as in the $k-\epsilon$ Model. So, this class of models performs better for flows with weak adverse pressure gradient and is better capable of predicting separated flows.

The main drawback of this model is its sensitivity to the free stream values and so the $k-\epsilon$ model presents a better performance near the boundary layer edge and away from walls (Moukalled et al., 2015) .

SST$-k-\omega-$ model

SST $k-\omega$ turbulence model combines best features from both $k-\omega$ and $k-\epsilon$ models. In such manner, its robustness is close to that of the $k-\omega$ model near wall surfaces and so its ability to compute flows with weak adverse pressure gradients accurately. On the other hand, it has a similar performance as the $k-\epsilon$ for modeling free shear flows or flows away from walls in the free-stream, avoiding the common $k-\epsilon$ problem that the model is too sensitive to the inlet free-stream turbulence properties. The SST $k-\omega$ model is commonly known for its good behavior in adverse pressure gradients and separating flow. However, large turbulence levels are encountered in regions with strong acceleration or stagnation regions. The previous phenomena is much less pronounced with a normal $k-\epsilon$ model.

3.5 Wall functions

As a turbulent flow approaches to a wall, the mean and fluctuating component of velocity, and consequently the turbulent kinetic energy k, vanish leading to large gradients. Therefore, if the near wall layer need to be resolved, a substantial number of grid points will be required. Resolving the viscous sublayer close to the walls is often very expensive.

Low Reynolds number turbulence models, such as the $k-\omega$, are capable of simulating the damping effects using a large number of grid points, but at the expense of unavoidable high computational costs if accurate solutions near wall region are required.

High Reynolds number turbulence models, such as the standard $k-\epsilon$ model, do not resolve the near wall layer, but wall functions are used for this purpose, reducing significantly the computational cost. Nevertheless, the main disadvantage of this approach is the validity of the theoretical profiles assumed between the boundary surface and the first near-wall node, which are only known and justified in near-equilibrium boundary layers. That is, the production and dissipation of turbulence kinetic energy are nearly equal. See works by Ferziger and Perić (2002) for a better understanding of these assumptions.

3.6 Standard wall functions

Theoretical assumed flow profiles can be divided into three regions that wall functions approach is based on, which encompasses the viscous sublayer ($0 < y^+ < 5$), the buffer sublayer ($5 < y^+ < 30$) and the inertial sublayer ($30 < y^+ < 200$), where y^+ is the normalized distance to the wall defined as follows

$$y^+ = \frac{d_\perp u_\tau}{\nu}, \tag{3.9}$$

with $d_\perp$ being the normal distance to the wall, ν the kinematic viscosity and u_τ the friction velocity expressed in the subsequent manner

$$u_\tau = \sqrt{\frac{|\tau_w|}{\rho}}, \tag{3.10}$$

where $|\tau_w|$ is the wall shear stress magnitude.

According to DNS and several measurements, it is known that viscous effects are small within the inertial sublayer, while turbulence is negligible in the viscous sublayer. On the other hand, both effects are important in the buffer sublayer with slightly dependency on the Reynolds number and the maximum turbulent production occurring. For this reason, low Reynolds number turbulence models place the first near-wall node in the viscous sublayer, while the practice of placing the first grid point in the inertial sublayer is adopted by high Reynolds number turbulence models (see Bredberg, 2000).

4 Problem definition

4.1 Dimensional analysis

For the purpose of solving the dependences of the problem under consideration, whose outline is presented in the following section, Buckingham π Theorem is applied. So, firstly, the main variables that govern our problem can be summarized as follows F, D, D_0', μ, V, ω, ρ and ϕ, so that

$$F = F\left(D, V, \omega, \mu, \rho, D_0', \phi\right), \tag{4.1}$$

where D represents the impeller diameter, V the ship velocity, ω the angular velocity of the impeller, μ the dynamic viscosity and ρ the density. Moreover, F is considered the resulting force acting on the impeller, ϕ the trailing edge (TE) pitch angle and D_0' the new venturi outlet diameter. The previous design variables have been defined in connection with further modifications that will be performed on the initial geometry. Then, according to Buckingham π Theorem, the number of parameters n appearing in the problem is $n = 8$.

The number of independent variables k representing length, mass and time is $k = 3$ so that the repeating variables in our case are ρ, ω, and D. Hence, the problem under consideration has $n - k = 5$ non-dimensional numbers defined as Π_1, Π_2, Π_3, Π_4 and Π_5.

$$\begin{aligned}
\Pi_1 &= \Pi_1\left(\rho, \omega, D, F\right), \\
\Pi_2 &= \Pi_2\left(\rho, \omega, D, V\right), \\
\Pi_3 &= \Pi_3\left(\rho, \omega, D, \mu\right), \\
\Pi_4 &= \Pi_4\left(\rho, \omega, D, D_0'\right), \\
\Pi_5 &= \Pi_5\left(\rho, \omega, D, \phi\right).
\end{aligned} \tag{4.2}$$

Now, taking under consideration the dimensions of each variable and using the MLT system, we have

$$\Pi_1 = \frac{F}{D^4\omega^2\rho}, \qquad \Pi_2 = \frac{V}{D\omega}, \qquad \Pi_3 = \frac{\mu}{\rho\omega D^2}, \qquad \Pi_4 = \frac{D_0'}{D}, \qquad \Pi_5 = \phi. \tag{4.3}$$

The functional relationship among the previous numbers may be expressed as

$$\frac{F}{D^4\omega^2\rho} = F\left(\frac{V}{D\omega}, \frac{\mu}{\rho\omega D^2}, \frac{D_0'}{D}, \phi\right). \tag{4.4}$$

Reynolds number and the normalized angular velocity of the impeller are defined in equations 4.5 and 4.6

$$Re = \frac{V_t D}{\nu}, \tag{4.5}$$

$$\Omega = \frac{\omega D}{V}, \tag{4.6}$$

where ν is the kinematic viscosity and $V_t = \omega D/2$ the impeller tip velocity. It is also convenient to define the following parameter

$$\Delta = \frac{D_0'}{D_0}, \tag{4.7}$$

where D_0 represents the initial venturi outlet diameter, so that the final relation between the resulting force and the main parameters governing our problem can be written as follows

$$C_f = f\left(\Omega, Re, \Delta, \phi\right), \tag{4.8}$$

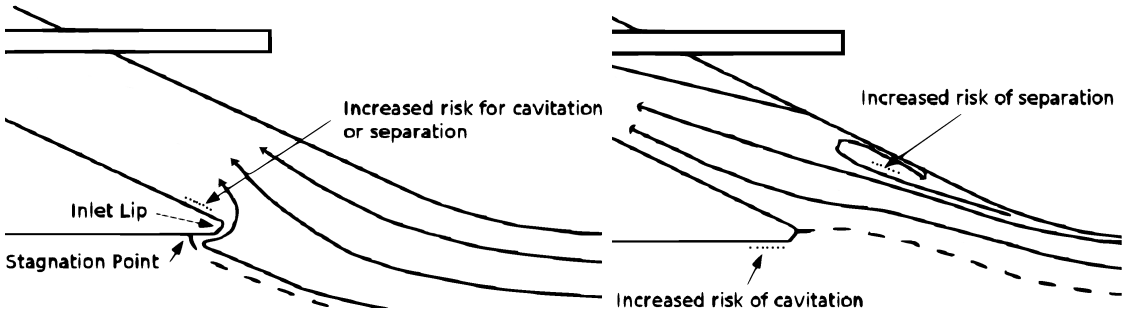

(a) Flow behavior when low IVR. (b) Flow behavior when high IVR.

Figure 4.1: Flow behavior at gullet inlet for different IVR values. Image from Bulten (2006).

where changes in the resulting force coefficients will be obtained by varying Ω as well as modifying the initial geometry through Δ and ϕ. Note that Reynolds number has been defined according to the impeller tip velocity, so that it will be kept constant throughout the computations.

In this part, specific velocities and standard parameters that are generally applied when studying jet-pumps are presented in order to describe the overall propulsion system behavior.

Several velocities can be distinguished when dealing with jet-drive systems: the ship velocity V, the averaged axial inflow velocity determined at the pump cross-section V_p and the averaged velocity at the venturi outlet V_0, defined in equations 4.9 and 4.10 respectively.

$$V_p = \frac{Q}{\frac{\pi}{4}D^2}, \tag{4.9}$$

$$V_0 = \frac{Q}{\frac{\pi}{4}D_0^2}, \tag{4.10}$$

where Q is the volumetric flow rate in m^3/s through the pump.

It is also important to define the inlet velocity ratio (IVR), which is a very significant parameter to describe flow phenomenas on jet-pumps. It relates the pump velocity V_p to the ship velocity V as follows

$$IVR = \frac{V}{V_p}, \tag{4.11}$$

IVR values are usually bounded between 0 and 2.5.

Flow behavior at different IVR values was predicted by Bulten (2006). At relatively low ship speeds the flow is accelerated when entering the gullet. Under this condition, the stagnation point of the dividing streamline is located at the hull side of the inlet lip or cutwater , which may lead to cavitation or separation at the upper side of the lip as shown in Figure 4.1a.

At normal operating conditions, IVR takes values from 1.3 to 1.8 for conventional water-jet systems, which implies a remarkable deceleration of the inflow. In this case, the stagnation point is situated at the inlet side of the lip as shown in Figure 4.1b. The limit at which these phenomenas occurs is fully dependent of the geometry under study.

On the other hand, the Jet Velocity Ratio (JVR) relates the velocity at the venturi outlet to the ship velocity as follows:

$$JVR = \frac{V_0}{V}. \tag{4.12}$$

The pressure coefficient must also be defined for the purpose of analyzing the subsequent results.

$$C_p = \frac{p - p_0}{\frac{1}{2}\rho V^2}, \tag{4.13}$$

considering the reference static pressure p_0 at the the intake tunnel inlet far upstream of the duct.

The following coefficients exhibited in equations 4.14 and 4.15 will be used in order to evaluate the generation of thrust and the torque required for the impeller respectively.

$$C_t = \frac{F_y}{\frac{1}{2}\rho V_t^2 A}, \tag{4.14}$$

$$C_m = \frac{M_y}{\frac{1}{2}\rho V_t^2 A D}, \tag{4.15}$$

where A represents the impeller area, F_y the resultant force and M_y the resultant torque or momentum acting on the impeller according to the reference coordinate system shown in Figure C.1 in Appendix C. Note that positive values of F_y are defined in the negative direction of the y-axis. Therefore, positive torque is defined by following the right-hand rule in the negative direction of the y-axis.

Two different values are usually defined for the Reynolds numbers when dealing with water-jet systems. Re for the impeller has been already presented in eq.4.5, which is based on V_t.

On other hand, the Reynolds number that characterizing the ship movement is defined as

$$Re_{in} = \frac{VD}{\nu}, \tag{4.16}$$

where, in this case, Re_{in} will fluctuate from 10^6 to 10^7, which can be regarded as high Reynolds number flow.

Even though simulations have been carried out for a constant angular velocity ω, the inlet flow angle seen by the impeller $\alpha = \text{atan}(2V_y/\omega D)$, being V_y the axial velocity seen by the impeller at each point. Figure 4.2 shows a schematic of the inflow velocity, which varies instantaneously for different ship velocities, leading to fluctuations of the impeller blade loading. Generally, lower inlet flow angles lead to higher blade loading.

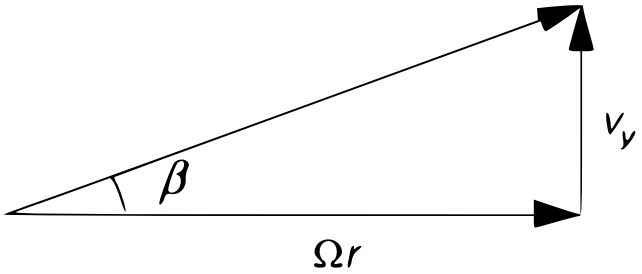

Figure 4.2: Velocity triangle for impeller inflow.

4.2 Problem formulation

First of all, the domain has been split into three main parts. The first, which remains still, is composed of the intake tunnel and the gullet. The region surrounding the impeller is included within the moving part. The rear part, composed of the stator, venturi and outlet will also remain static. So two coupled adjacent surfaces, which will slide along each other, are defined to separate rotating and static regions. (see Appendix A for a more in detailed review of how this problem have been tackled in OpenFOAM®)

An outline of the computational domain under consideration can be observed in Figure 4.3. Note that the tunnel has been generated in order to simulates the inflow for a full scale jet-pump installation, allowing the proper BC to be imposed on that region and so representing the ship velocity. In such manner, it has been included for the sake of consistency and physics of the model. Previous studies and experimental data obtained by Bulten (2006); Peixin and Mehrdad (1999), which evaluates the influence of the intake tunnel over the resulting flow pattern using the $k-\epsilon$ model, have been taken into account in order to establish the dimensions for its domain as well as an approximation to its corresponding mesh resolution. All parts defining the jet-pump under study are sketched in Figure 4.3.

On the other hand, with regard to the parameters that govern our problem, values for Ω, defined in eq. 4.6, are bounded between 5 and 33 in order to study the overall performance of the system. So IVR index will take values from 0.42 to 2.17, corresponding to Ω values of 33 and 5 respectively. Note also that computations have been carried out fixing Reynolds number constant at $Re = 10^7$ according to equation 4.5, since the angular velocity of the impeller is kept constant. The previous values have been established considering normal operating conditions for a typical PWC and considering similar studies performed on water-jet systems such as those by Bulten (2006); Peixin and Mehrdad (1999). On the other hand, values for ϕ and Δ are bounded as follows: $19^o \leq \phi \leq 28^o$ and $0.77 \leq \Delta \leq 1.28$, for the purpose of analyzing the resulting thrust and momentum coefficient.

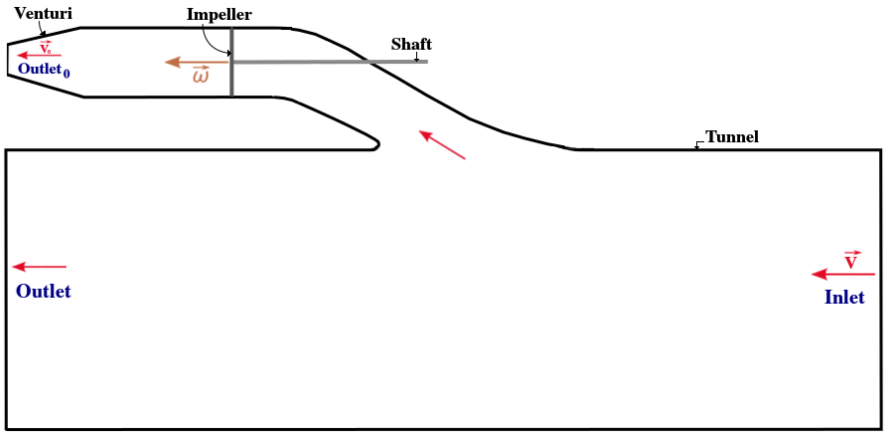

Figure 4.3: Domain sketch.

In order to get a better approach to the real problem under consideration and so as to get a more accurate solution, nearly every component of the jet-pump under study will be modeled. They all have an influential position within the flow behavior and the resulting propulsion generation. Nevertheless, some assumptions will be taken into account with regard to these parts when running the computations.

- Firstly, the nozzle will not be considered. The function of the nozzle is redirecting the trajectory of the jet-pump output flow so as to steer the craft, but, since it keeps the venturi section area and the operating conditions for the simulations are at cruise speed without maneuvers, this component will not be modeled.

- The intake grate or scoop grate, which is mounted on the bottom of the hull at the gullet inlet and prevents foreign objects from entering to the jet pump, is not modeled either. Recent studies about water-jet system show reliable results without considering the intake grate, e.g. (see Bulten, 2006; Park et al., 2005a,b).

- Although in the real problem the Drive Shaft rotates in conjunction with the impeller, it will be assumed still in order to decrease computational costs. So only the domain associated to the impeller will be deforming and moving during the simulation. Peixin and Mehrdad (1999) exhibit an analysis comparing the influence of the presence of the shaft, stationary and rotating, as well as its absence at several operating conditions. Analyzing the flow behavior near to the inlet for different operating conditions of the shaft, it is observed that the presence of the shaft, even when stationary, has a significant effect on the flow field even far upstream of its location in comparison to the same without shaft. On the other hand, only when Reynolds number is small the effect of the shaft rotation is large. So, it is conclude that a stationary shaft must be included in the computational model.

- Finally, all of the geometries generated on this work are based on measures that have been carried out directly over the physical parts shown in Appendix B. Due to the difficulty of measuring accurately the large number of complex surfaces that make up the jet-pump, it is important to notice that this is an approach to the real domain and proper planes of the parts under study would be necessary so as to get more accurate solutions to the real problem.

In analyzing the problem under consideration, a solid body under rotation and sunk in water, it is important to determine the type of flow that it is being dealt with. So the fluid flow behavior can be categorized as Newtonian, three-dimensional, single phase, transient, viscous and incompressible. On the other hand, the body under study will be supposed a rigid solid with material properties remaining constant.

4.3 Computational domain

A previous step in order to achieve a relevant geometry from the CFD perspective involves a description of the body surface under study.

The subsequent presented geometry has been modeled based on the propulsion system for a *PWC Bombardier xp 951 99* (see Appendix B). All the necessary measures have been obtained by directly gaging the physical parts by means of calipers and a pitch gauge for the impeller. Considering the measures gathered in table C.1 (Appendix C), a geometric representation of these parts can be observed on the figures below (see Appendix D for a deeper review of the geometry generation procedure).

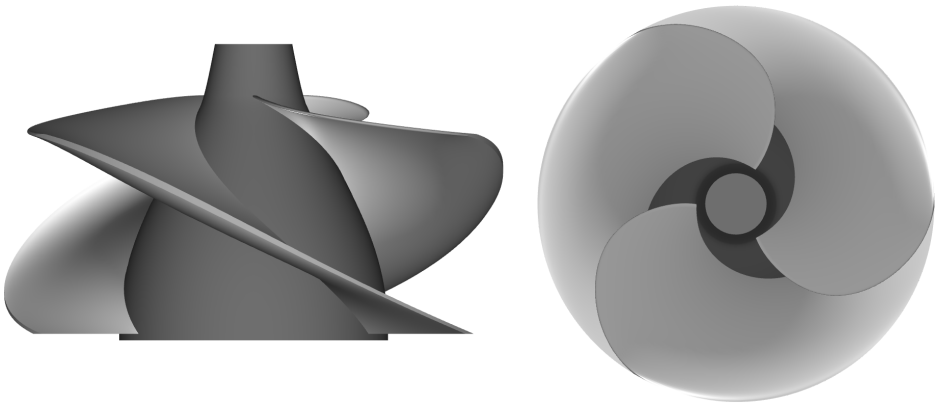

(a) Modeled impeller, side elevation. (b) Modeled impeller, plan view.

Figure 4.4: Modeled impeller.

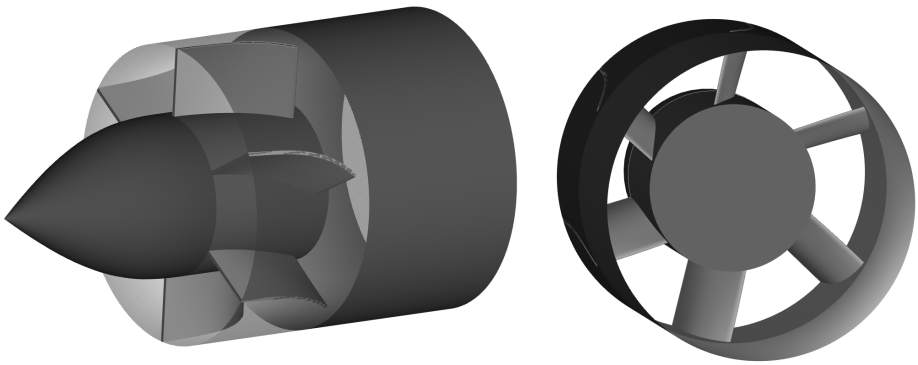

(a) Modeled stator and vanes, side Elevation. (b) Modeled stator and vanes, front Elevation.

Figure 4.5: Modeled stator and vanes.

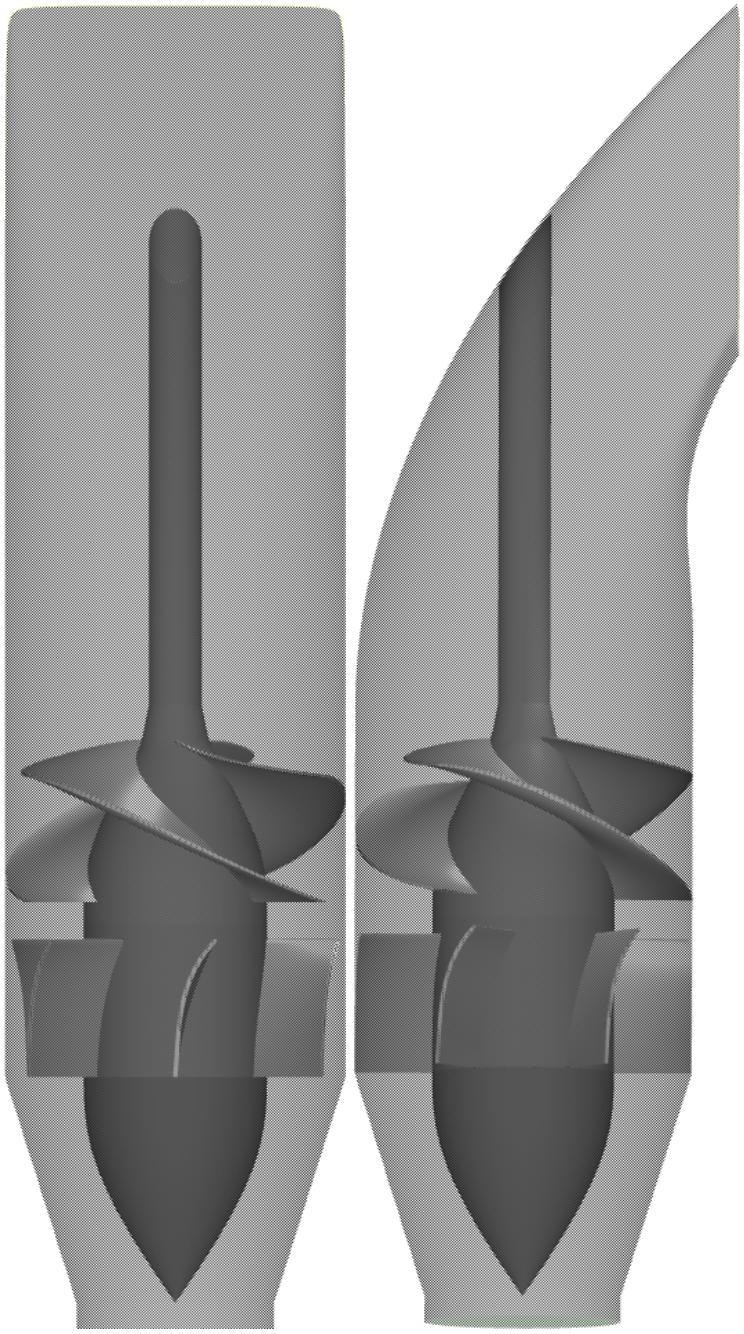

(a) Modeled jet-pump, plan view.

(b) Modeled Jet-pump, side elevation.

Figure 4.6: Modeled jet-pump.

4.4 Boundary Conditions

The discretized domain is bounded by several surfaces where different types of boundary conditions (BC) must be imposed. In this section, a brief conceptual review is carried out on how these BC are prescribed (see Appendix A to review how they have been implemented within OpenFOAM). It is also important to highlight that, even though the initial conditions for the internal field must also be defined, they can be considered more of an initial guess of the solution in order to aid in convergence, as guesses excessively far from

the appropriate solution may lead to solver divergence. In this case, as can be observed in Table 4.1, initial value of the internal field for the pressure and velocity distribution are initially set to 0.

Flow Field	Velocity $\vec{U}(m/s)$	Pressure p/ρ (m^2/s^2)
Initial Value	0	0
Boundary Condition at:		
Tunnel Inlet	$V\vec{e_y}$	$\frac{\partial p}{\partial \vec{n}} = 0$
Tunnel Outlet	$\frac{\partial \vec{U}}{\partial \vec{n}} = 0$	0
Tunnel Walls and Shaft	$slip$	$\frac{\partial p}{\partial \vec{n}} = 0$
Impeller	$\frac{\omega D}{2}(\sin\theta\vec{e_x} - \cos\theta\vec{e_z})$	$\frac{\partial p}{\partial \vec{n}} = 0$
Jet-Pump Outlet	$\frac{\partial \vec{U}}{\partial \vec{n}} = 0$	0
Walls left	0	$\frac{\partial p}{\partial \vec{n}} = 0$

Table 4.1: Boundary Conditions scheme for U and p.

where θ is considered positive following the right-hand rule on the y-axis and starting from the x-axis. The vector $\vec{n}$ denotes the unit normal vector to the surface under consideration.

Firstly, the ship velocity V at the tunnel inlet, normal to the inlet plane, is prescribed with a constant value and uniform distribution throughout the plane, since $\frac{\partial p}{\partial \vec{n}} = 0$.

At the tunnel outlet, a constant value for the static pressure is prescribed over the whole plane. It is assumed that the static pressure is uniform at large enough distance from the waterjet inlet. The same condition applies for the venturi or jet-pump outlet. However, the resulting velocity distribution will be non-uniform.

Since the shape for the craft hull is unknown and its study is beyond the scope of this analysis, the boundary layer velocity profile for the hull at the intake tunnel is neglected by using a slip type boundary condition on the tunnel walls. So, the velocity value at the wall will be the same as the near wall component. This fact allows a mesh near these walls relatively coarse, since the boundary layer is not resolved. Moreover, since the flow cannot go into the wall, $\frac{\partial p}{\partial \vec{n}} = 0$, making the velocity tangent at every point on the wall. The drive shaft will adopt the same boundary conditions since it will be supposed stationary.

The flow on the impeller is computed in a stationary frame of reference, so the velocity vector $\vec{U}$ must equal the impeller velocity at each point over its surface so that $\vec{U} = 0$ relative to the impeller surface, fulfilling the no-slip condition. On the other hand, $\frac{\partial p}{\partial \vec{n}} = 0$ must also be fulfilled since the impeller is also a wall.

A wall boundary condition is applied to the remaining surfaces, where pressure gradi-

ent also set to zero in normal direction.

Flow Field	$k\,(m^2/s^2)$	$\epsilon\,(m^2/s^3)$
Initial Value	0.06	0.0495
Boundary Condition at:		
Tunnel Inlet	0.06	0.0495
Tunnel Outlet	$\frac{\partial k}{\partial \vec{n}} = 0$	$\frac{\partial \epsilon}{\partial \vec{n}} = 0$
Jet-Pump Outlet	$\frac{\partial k}{\partial \vec{n}} = 0$	$\frac{\partial \epsilon}{\partial \vec{n}} = 0$
Walls left	kqRWallFunction	epsilonWallFunction

Table 4.2: Boundary Conditions scheme for k and ϵ.

Finally, table 4.2 exhibits an overview of the BC applied to the parameters of turbulence modeling. It can be observed that wall functions are used to model the velocity profile at the first node to the wall on each case, while a fixed value is imposed at the tunnel inlet according to similar studies (see Bulten, 2006).

5 Numerical method

5.1 Mesh generation

In general, a geometric domain may be discretized using either a structured or an unstructured mesh. A series of considerations will be contemplated in order to choose the proper type of mesh. First af all, in a structured mesh, the elements are defined by their local indexes as shown in Figure 5.1a, which involves a significant advantage for the numerical method when accessing each element and its adjacent cell and so accelerating the meshing process.

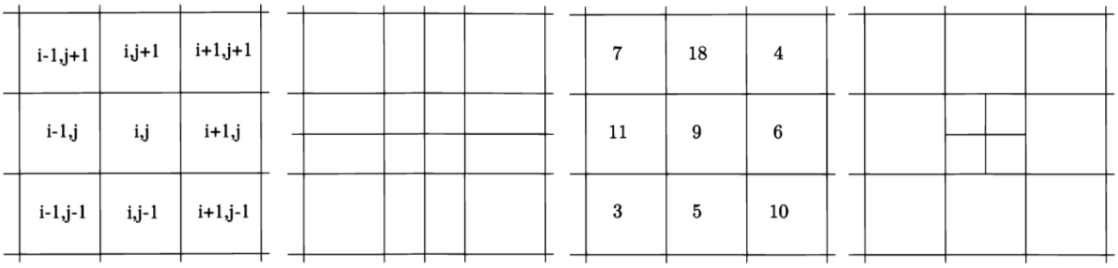

(a) Structured mesh. (b) Structured refined mesh. (c) Unstructured mesh. (d) Unstructured refined mesh.

Figure 5.1: Comparison between structured and unstructured meshes. Image from Maric et al. (2014).

On the other hand, it must be taken into account that a dense mesh must be generated where large gradients occur to avoid large jumps in the values of physical properties, not wasting cells in flow regions where no such gradients occur. However, refining the mesh locally is impossible to achieve with structured meshes since the refinement is propagated into the respective direction through the entire mesh in order to maintain its topology (Figure 5.1b). On the other hand, even though structured meshes may increase the accuracy of the numerical solution due to the arrangements of their cells, they are less flexible when used for complex geometries.

There are multiple open source mesh generators designed specifically for OpenFOAM® that can be used. The most commonly known are `blockMesh` and `snappyHexMesh`. The first generates a block-structured hexahedral mesh which is rather tedious to handle for complex geometries so that `snappyHexMesh` will be used for this purpose. However, `blockMesh` is a great tool for generating background meshes required by snappy, so it will be used for this purpose.

`SnappyHexMesh` requires two previous steps, the geometry of the body surface must be generated, which is shown in the previous section, and a background hexahedral mesh must be created. `blockMesh` is executed to create the background mesh. Below it is shown the set of parameters that controls the quality of the background mesh, which is composed of 7 blocks. (See Appendix A for further information of the meshing procedure).

Cells control parameter	Number of cells
S_x	20
S_z	96
S_y	24
B_x	6
B_y	16
B_z	16

Table 5.1: Main configuration parameters for background mesh.

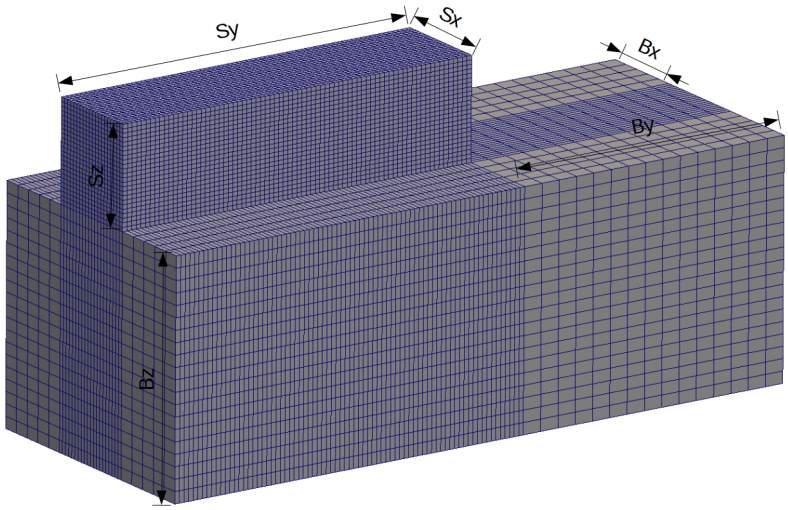

Figure 5.2: Hexahedral background mesh.

where, according to the dimensions of the domain under study, the following relations must be fulfilled, $S_z = 1.2S_x$ and $S_y = 4.8S_x$, in order to maintain the cell ratio equal to 1 and so enhancing the meshing procedure by `snappyHexMesh`. In such manner, $B_z = B_y = 2.6B_x$ must be also satisfied.

A brief summary of the main parameters that control the quality of the final mesh is exhibited below.

Refinement surface	Level
Tunnel	(0 0)
DriveShaft	(1 2)
Gullet	(1 2)
Impeller_Hub	(2 3)
Impeller_Blades	(3 3)
Shroud	(2 2)
Stator_Core	(2 3)
Stator_Vanes	(3 3)
Cone	(2 2)
Venturi	(1 2)

Table 5.2: Main refinement parameters for `snappyHexMesh`.

The computational grid shown in Figure 5.3 derives from the selection of the previously

shown refinement levels. These parameters will depend on several factors such as the convergence and accuracy of the results or the associated computational cost. A convergence analysis is performed by means of Richardson Extrapolation method in order to estimate the values for these parameters (see Appendix E).

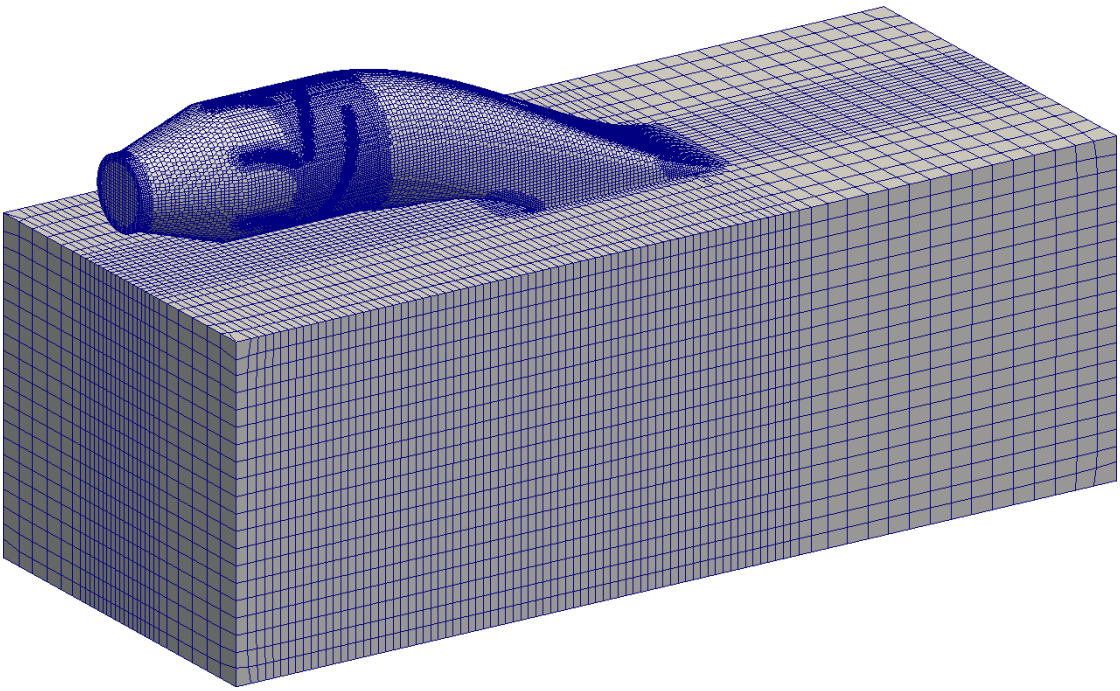

Figure 5.3: Final computational grid.

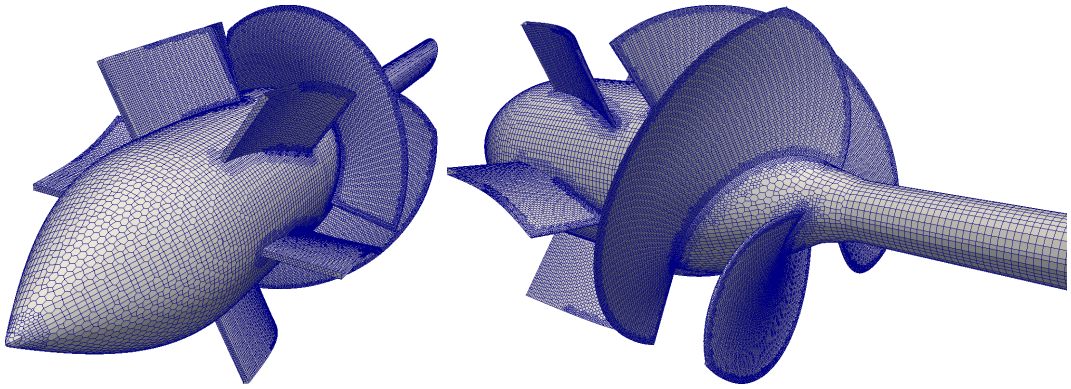

(a) Mesh rear view. (b) Mesh front view.

Figure 5.4: Mesh inside view.

Adjacent surfaces separating rotating and static regions are shown in Figure 5.5. (See Appendix A for a more in detail review of how this separation have been performed in OpenFOAM®)

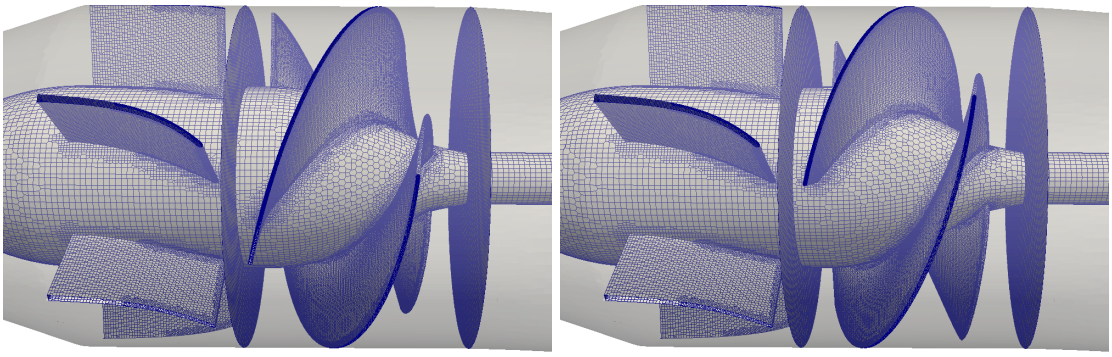

(a) Initial time step. (b) Later time step.

Figure 5.5: Dynamic mesh exhibition.

5.2 Numerical schemes

In this case, the solver `pimpleDyMFoam` will be used, which is based on a hybrid approach composed of PISO and SIMPLE algorithms (see Jasak (1996) for a deeper explanation of both algorithms). The solver `pimpleDyMFoam` is a transient solver for incompressible, Newtonian flows on a moving mesh. A geometric-algebraic multi-grid (GAMG) solver is used for the pressure equation while the solver smooth solver works out the equations left. On the other hand, the temporal integration was performed by using a implicit, first order, Euler scheme. The spatial discretization for gradient, divergence and laplacian terms was warried out with a central second order differencing scheme. First order upwind differences were applied to the turbulence parameters k, ϵ and ω.

On the other hand, the time step of the simulation has been set according to the Courant-Friedrich-Lewy (CFL) number, which represents a numerical constraint to the maximum allowed time step for a specific grid size. This condition is very necessary for convergence of the results. So, the value for the time step δt has been given in order to maintain a maximum Courant Number smaller than 1, according to the following equation.

$$C_{max} = \frac{u_{max}\delta t}{\delta x_{min}} \leq 1 \tag{5.1}$$

where u_{max} denotes the maximum velocity reached within the computational domain and δx_{min} the smallest grid spacing that can be found in the mesh.

On the other hand, all calculations presented in the present work have been carried out for a constant angular velocity of the impeller, where the Arbitrary mesh interface (AMI) algorithm is used to model its rotating motion.

According to explanations from previous sections, $k - \epsilon$ model is used due to computational constraints and similar studies for water-jet systems.

6 Results and discussion

6.1 Stagnation point and flow behavior near the inlet

In order to study the overall performance of the system under consideration, the current analysis will be focused on the flow pattern for the gullet.

Computations have been performed maintaining $Re = 10^7$ constant, according to eq. 4.5 and considering values for normal operating conditions. Values of $\Omega = 33.3$, $\Omega = 14.3$, $\Omega = 6.7$ and $\Omega = 5$ have led to IVR=0.42, IVR=0.89, IVR=1.22 and IVR=2.17 respectively, according to Eq. 4.11. The velocity vectors of the flow field near to the gullet entrance are presented in Figs. 6.1.

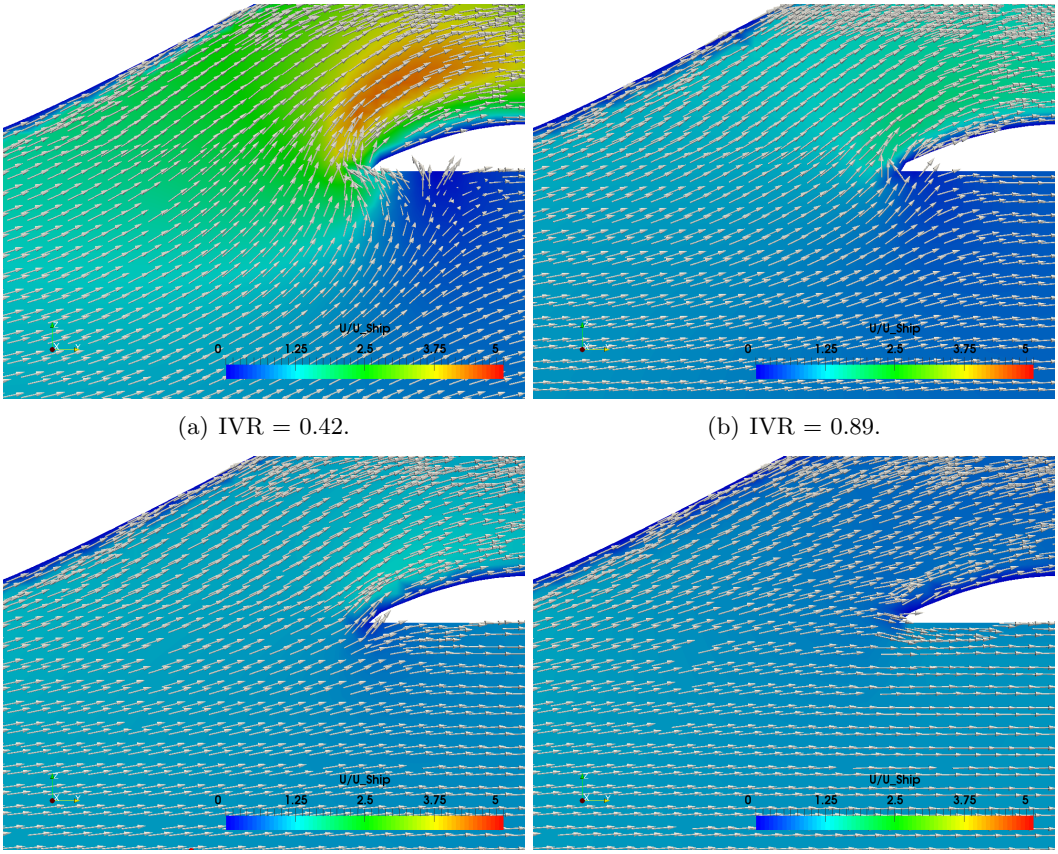

(a) IVR = 0.42.

(b) IVR = 0.89.

(c) IVR = 1.22.

(d) IVR = 2.17.

Figure 6.1: Velocity vectors of the fluid near the duct lip.

Note that previous and succeeding snapshots have been taken for a dimensionless time $\tau = t\omega = 12$, when the impeller has rotated two revolutions approximately. On the other hand, values for time dependent variables have been averaged as follows

$$\overline{\Phi} = \frac{1}{\Delta\tau}\int_{\tau_0}^{\tau+\Delta\tau} \Phi(\tau)d\tau, \tag{6.1}$$

where $\tau_0 = 0$ and $\Delta\tau = 5$. On the other hand, Φ represents variables such as the thrust or momentum coefficient C_t and C_m, or velocities such as the pump velocity V_p.

When the IVR takes values from 0.42 to 0.89, the stagnation point is located at the hull side of the inlet lip (or cutwater), the tendency to flow separation near the duct lip can be observed, forming low pressure zones near the lip and making cavitation possible. When Re_{in} is increased, IVR takes values from 1.22 to 2.17. In this case, the stagnation point is moved to the upside of the duct lip and simultaneously the tendency of the flow to separation near the inlet in Fig 6.1(c) is decreased in comparison of that in Fig. 6.1(a). There is a point in which the stagnation point is situated on the upper side of the lip and there is no possibility to separated flow near the cutwater.

This phenomena was also observed by Peixin and Mehrdad (1999) when analyzing the separated flow inside a water-jet intake duct under different operating conditions and obtaining similar results. Note that definition of the IVR is different for some authors, who define the inlet velocity ratio as $IVR = V_p/V$. The results obtained by this author are summarized in Fig.6.2 according to eq. 4.11 for IVR. Note that the stagnation point is strongly influenced by the geometry of lip shape.

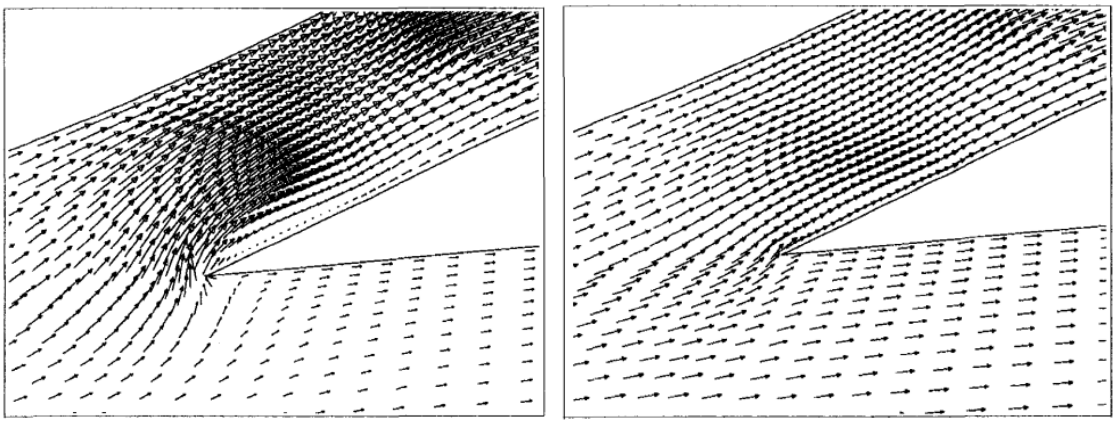

(a) IVR = 0.45. (b) IVR = 1.21.

Figure 6.2: Velocity vectors of the fluid near the duct lip. Image from Peixin and Mehrdad (1999).

It is concluded that the IVR has an important effect on the flow separation, the formation of low pressure zones near the cut-water and the cavitation phenomena. When IVR is small enough, separated flow near the cutwater might occur and when IVR is large enough there is no separated flow in that region.

6.2 Performance of the system

Pressure Coefficient analysis

The results obtained for the pressure coefficient, measured along the ramp center line starting from the duct inlet to the plane just upstream of the impeller, are shown according to eq. 4.13. The computational results are compared afterward to those achieved by Bulten (2006), who also performed a comparison between CFD and experimental results based on measures to the static pressure along the ramp centre line at 12 different locations.

The pressure coefficient is analyzed in Figure 6.3 and 6.4 at several operating conditions where IVR index takes values from 0.54 up to 2.17. Re_{in} defined in eq. 4.16 will be in the order of $4x10^6$ to $2x10^7$ respectively.

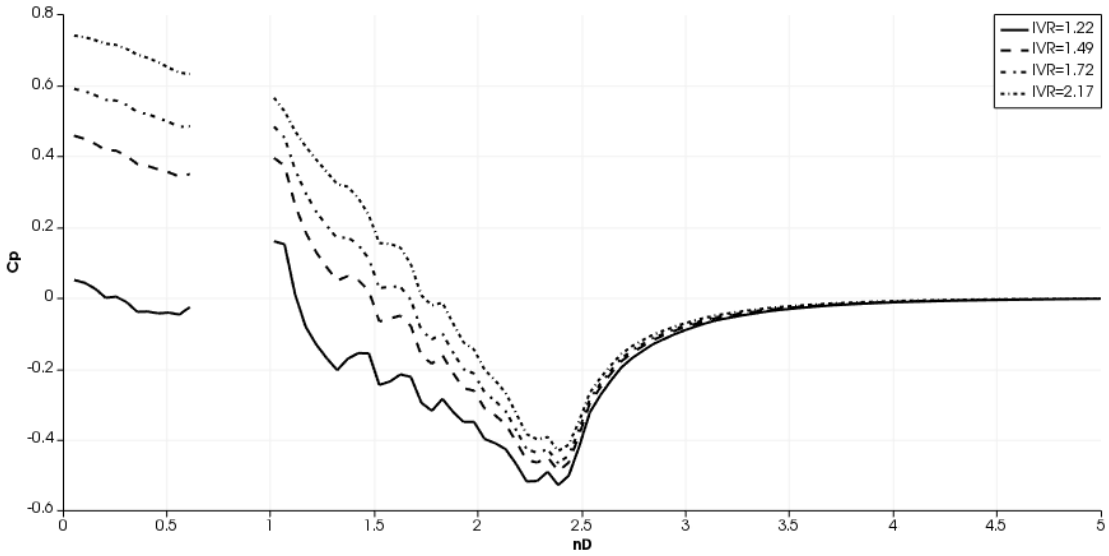

Figure 6.3: Pressure coefficient at different IVR values along the duct ramp center line for IVR fom 1.22 to 2.17.

where values for x-axis are given as a function of the distance from the impeller plane n times the impeller diameter D.

The discontinuity in calculated pressure coefficient from 0.5D to D is due to the presence of the shaft. On the other hand, the value for the pressure coefficient at the impeller plane in Figure 6.3 increases with increasing values of IVR due to negative increments of the velocity gradient as the fluid flows into the gullet. The opposite effect occurs in Figure 6.4.

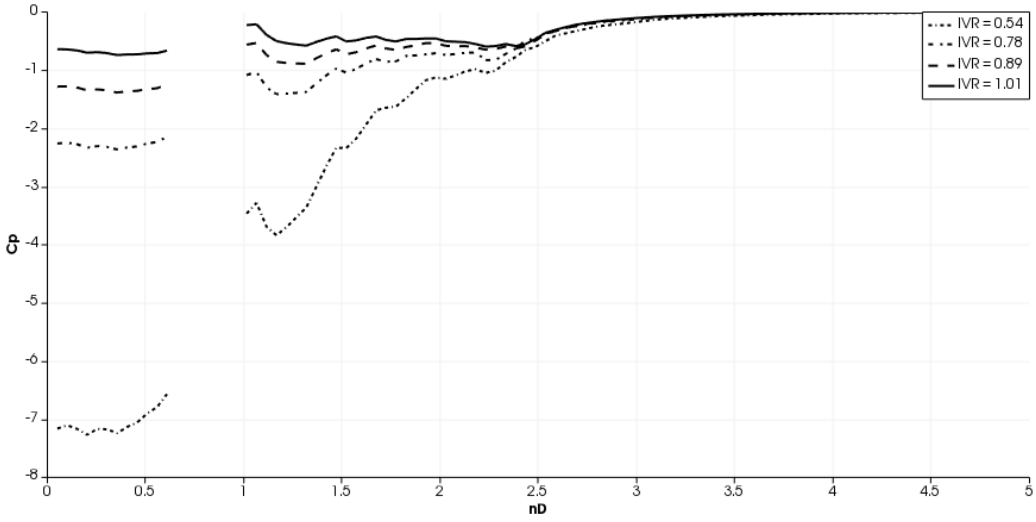

Figure 6.4: Pressure coefficient at different IVR values along the duct ramp center line for IVR fom 0.54 to 1.01.

where the lower the IVR index the larger the absolute value for the pressure coefficient in Figure 6.4. That is, the vacuum generated by the impeller, for the same angular velocity, is more effective since Re_{in} is smaller and the flow accelerates its way in, even more

when lower values for the IVR. Previous results are also illustrated in Figure 6.8.

Bulten (2006) carried out a similar analysis only for those IVR values that are included within the range from 1.21 to 2.19, whose results are shown in Figure 6.5.

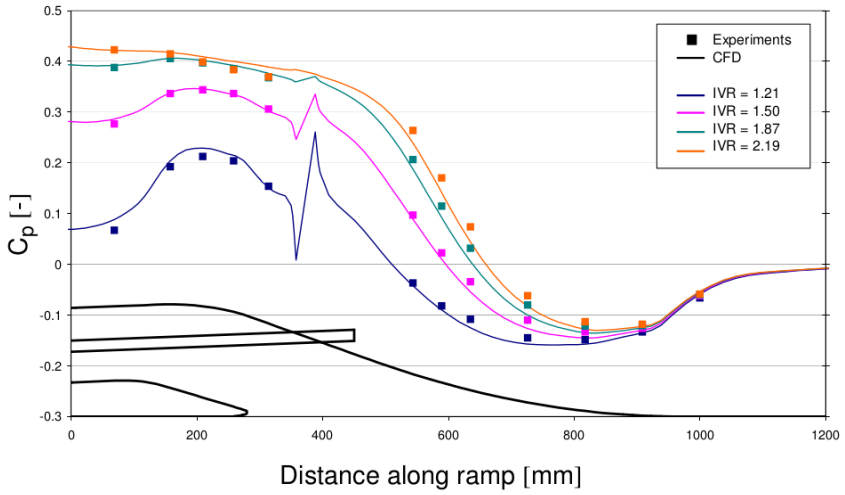

Figure 6.5: Comparison of experimentally measured and calculated pressure coefficient along the ramp centre line. Image from Bulten (2006).

where values are given as a function of the distance from the impeller plane.

Note that both geometries are different. In figure 6.5, the radius for the beginning of the ramp is larger and so it is less curved. Consequently, the flow behavior in that region is different for the same in Figure 6.3 so that absolute value for the pressure coefficient is smaller in Figure 6.5. On the other hand, note that at the end of the curves in Figure 6.5, the bottleneck and so the pressure coefficient decreases at lower values of IVR. This is produced by a arrangement where the impeller is not right after the end of the duct outlet and there is a small extension to the gullet. In Figure 6.3, the plane just upstream of the impeller where the measures begin is situated right after the duct outlet. Finally, different values for the pressure coefficient at this plane can be justifies by differences in both ducts representations since the operating conditions are the same.

Despite of differences in both geometries and propulsion systems characteristics, both figures 6.5 and 6.3 show a good agreement for the flow behavior between studies, so that the results obtained by this author keep similarity and are consistent enough to confirm the validity of our results.

The results are also compared to those obtained by Park et al. (2005a), who performs a numerical analysis of a a water-jet propulsion system by means of the $k-\epsilon$ turbulence model in a commercial CFD software. Experimental data is also used to validate the results obtained for the pressure coefficient. This time, the pressure is measured at the ramp side of the duct for IVR = 0.6 constant. Figure 6.6 represents the points where the static pressure have been measured by Park et al. (2005a) in order to obtain the values for the pressure coefficient shown in Figure 6.7. Figure 6.10 shows results in a three-dimensional standpoint under this operating condition.

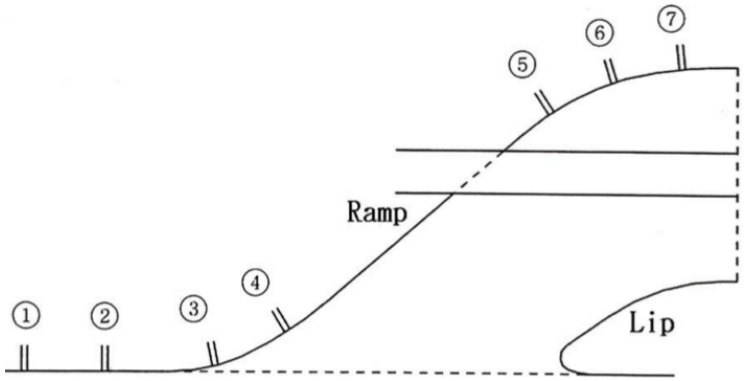

Figure 6.6: Surface reference for pressure coefficient measurement through experimentation. Image from Park et al. (2005a)

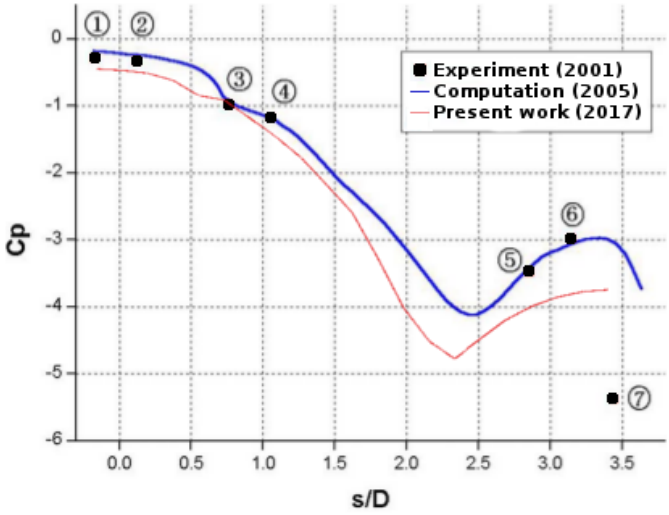

Figure 6.7: Comparison between numerical and experimental data for pressure coefficient at gullet for IVR=0.6.

Note that the reference point to start the measures matches the point number 1 in Figure 6.6. On the other hand, the pressure coefficient has been measured on a plane that is displaced from the shaft axis and so the discontinuity does not appear in this case. In Figure 6.4 can be observed a peak right before the discontinuity, which cannot be seen in Figure 6.7 since this fact coincide with the flow running into the shaft and its associated increasing value for the pressure coefficient, which does not occur in Figure 6.7.

The duct as well as the shaft dimensions from the referenced author have some similarities with regard to the same for the present work, but their shapes are still different. Despite of this fact, the results achieved in the present work are still consistent with those obtained in previous analysis and experimentation by Park et al. (2005a), confirming their validity.

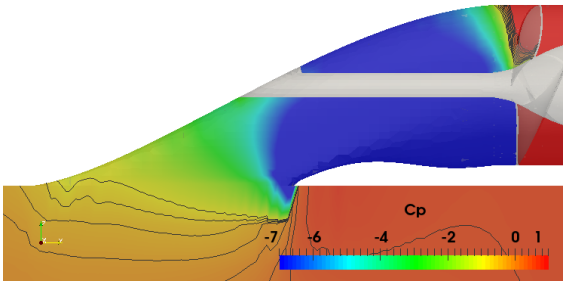

(a) IVR = 0.54, $Re_{in} = 4 \cdot 10^6$.

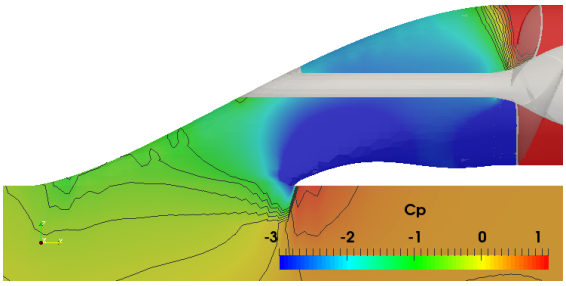

(b) IVR = 0.78, $Re_{in} = 6 \cdot 10^6$.

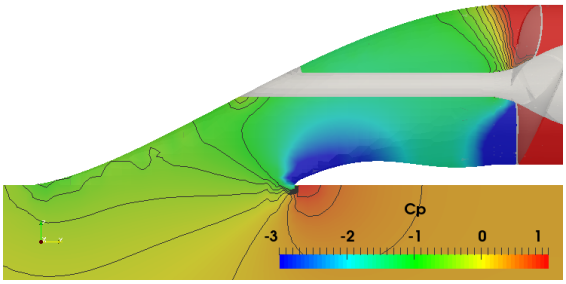

(c) IVR = 0.89, $Re_{in} = 7 \cdot 10^6$.

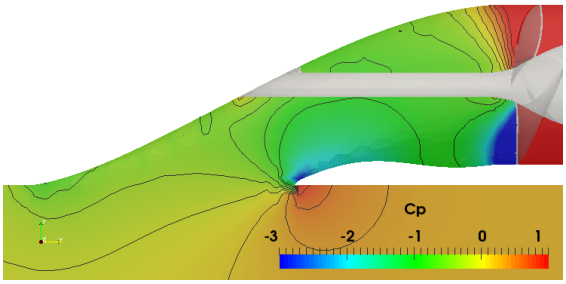

(d) IVR = 1.01, $Re_{in} = 8 \cdot 10^6$.

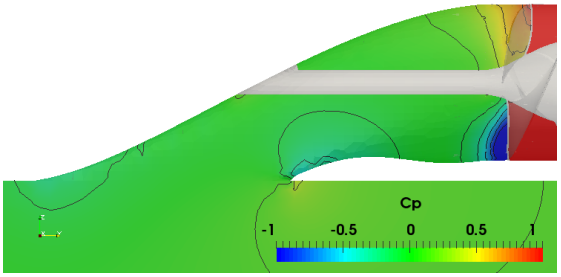

(e) IVR = 1.22, $Re_{in} = 1 \cdot 10^7$.

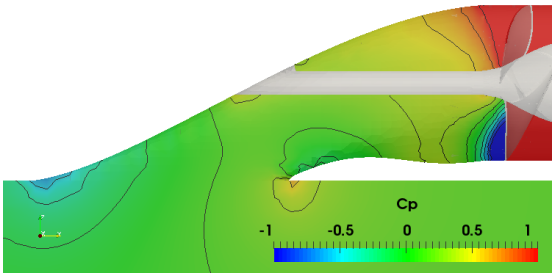

(f) IVR = 1.49, $Re_{in} = 1.3 \cdot 10^7$.

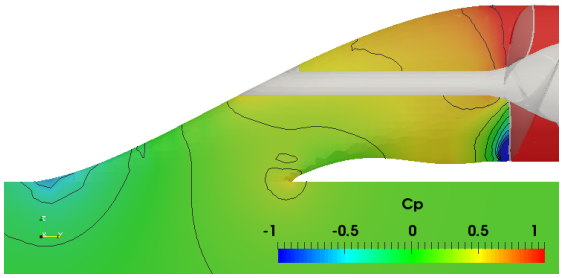

(g) IVR = 1.72, $Re_{in} = 1.5 \cdot 10^7$.

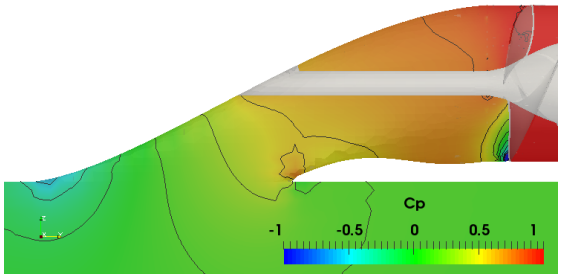

(h) IVR = 2.17, $Re_{in} = 2 \cdot 10^7$.

Figure 6.8: Pressure coefficient at different operating conditions along the duct.

Peixin and Mehrdad (1999) compared the pressure coefficient at the plane just upstream of the impeller to experimental data preliminary gathered for similar conditions, which agree to the previously shown computational results. Values for the pressure coefficient at the cross-section right before the impeller have been measured and overlapped to those obtained by Peixin and Mehrdad (1999) in Figure 6.9.

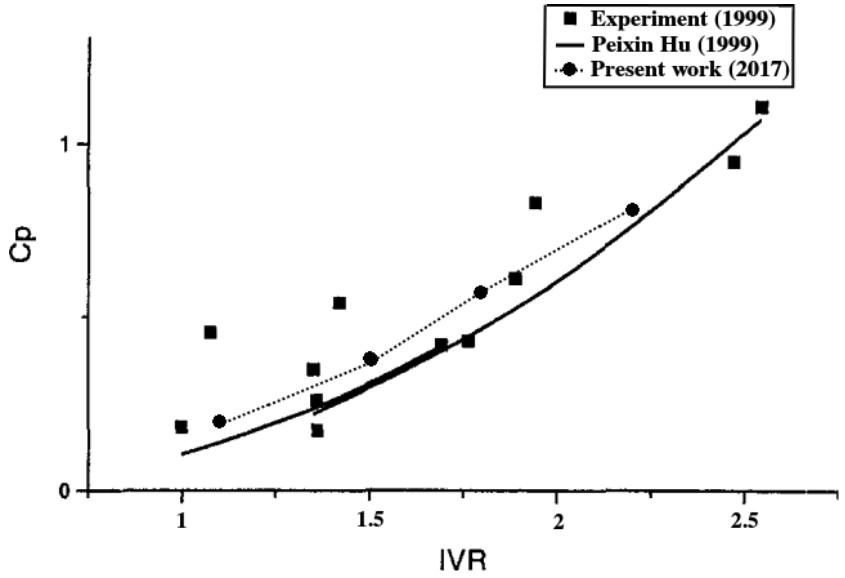

Figure 6.9: Comparing numerical and experimental data for pressure difference coefficient at plane upstream of the impeller

In conclusion, when IVR is less than 1 and Re_{in} is increased, the initial vacuum exhibited by the impeller at the duct inlet is less "effective". More vacuum is needed in order to keep the same pressure loss since it decreases when greater IVR values occur for the same angular velocity of the impeller. When IVR is greater than 1, a bottleneck effect is generated whose intensity becomes larger as the IVR value is increased. This fact makes the torque required by the system increase when Re_{in} is smaller as the impeller effort to "absorb" water is also increased. This statements are also confirmed by Peixin and Mehrdad (1999). However, the performance or power to produce thrust decreases in general, which can be observed in the following section.

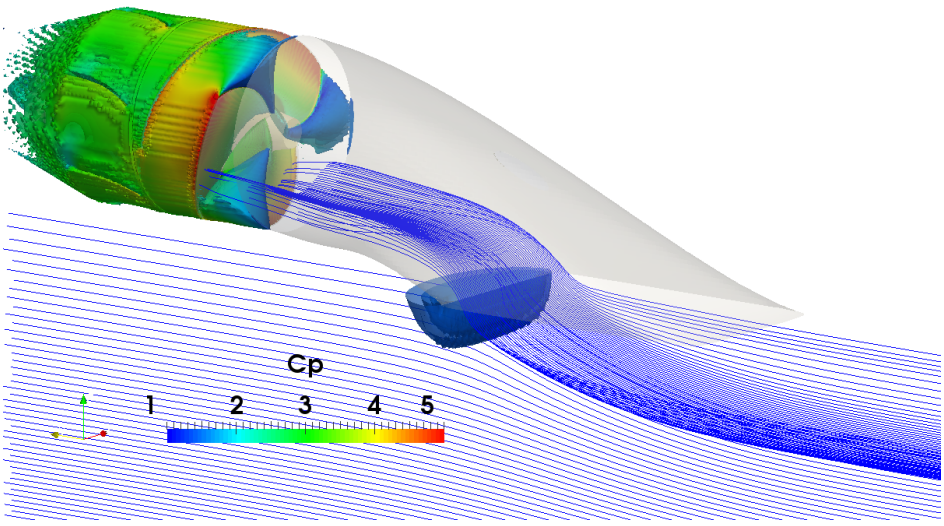

Figure 6.10: Pressure Coefficient throught jet-pump.

Thrust and Momentum generation

Thrust generation at different operating conditions have been compared to those obtained by Bulten (2006), who studied the deviation of the normalized thrust with a given design thrust for a constant angular velocity of the impeller. Both results are overl apped in Figure 6.11.

It can be observed how the thrust coefficient decreases as the ship velocity is increased. This fact can be explained by means of the previous explanation for the pressure coefficient variation at different operating conditions, shown in Figure 6.4. Since the impeller velocity is remained constant, the pressure difference between the blade face and the blade back decrease and so the generated thrust. On the other hand, note that, when $V = V_{ship}$ is increased, the axial velocity at the duct outlet is also increased (see Figure 6.12) and the inflow angle seen by the impeller becomes larger. This fact leads to smaller loading of the impeller blades, resulting in less torque required, since the momentum coefficient decreases, but the jet-pump power for producing thrust is also decreased, as shown in Figure 6.11.

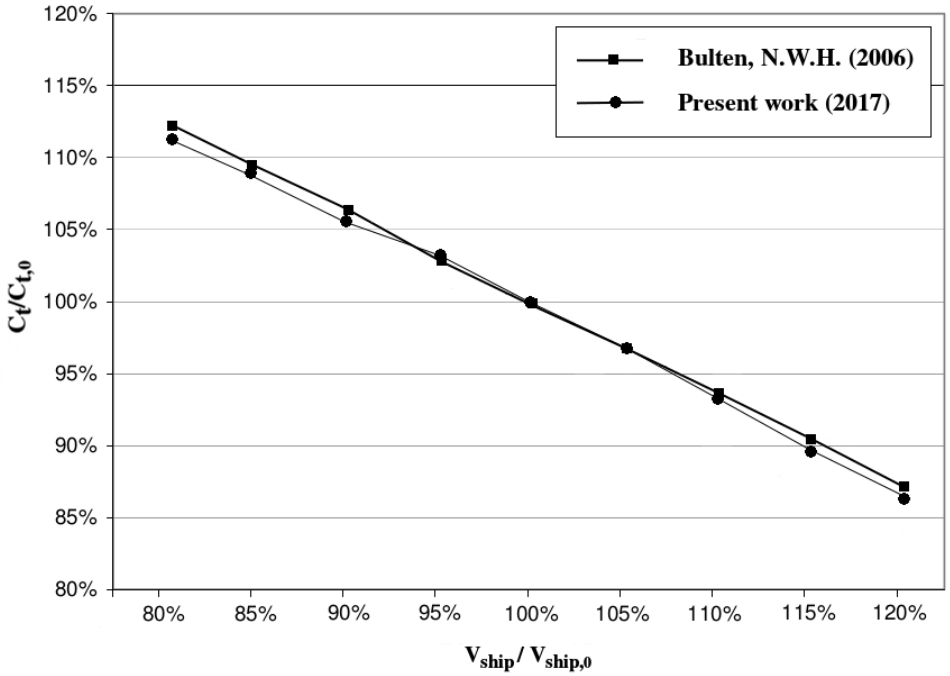

Figure 6.11: Thrust variation at different operating conditions.

where $C_{t,0}$ represents the thrust coefficient at $\Omega = 10$. These results can also be inferred from Table 6.1.

Ω	Re_{in}	IVR	V_p/V_t	Q^*	V_o/V_t	C_m	C_t
5.0	$2.0 \cdot 10^7$	2.17	0.185	0.184	0.55	0.082	0.615
5.9	$1.7 \cdot 10^7$	1.91	0.178	0.178	0.53	0.089	0.677
6.3	$1.6 \cdot 10^7$	1.81	0.176	0.176	0.52	0.091	0.695
6.7	$1.5 \cdot 10^7$	1.72	0.174	0.174	0.52	0.093	0.714
7.8	$1.3 \cdot 10^7$	1.49	0.174	0.174	0.51	0.100	0.788
10	$1.0 \cdot 10^7$	1.22	0.164	0.164	0.49	0.102	0.796
11	$9.0 \cdot 10^6$	1.11	0.162	0.161	0.48	0.104	0.812
12	$8.0 \cdot 10^6$	1.01	0.159	0.159	0.47	0.105	0.827
14	$7.0 \cdot 10^6$	0.89	0.156	0.155	0.46	0.106	0.841
16	$6.0 \cdot 10^6$	0.78	0.153	0.153	0.45	0.107	0.851
20	$5.0 \cdot 10^6$	0.66	0.150	0.150	0.44	0.108	0.859
25	$4.0 \cdot 10^6$	0.54	0.147	0.147	0.43	0.108	0.861
33	$3.0 \cdot 10^6$	0.42	0.144	0.144	0.42	0.109	0.862

Table 6.1: Propulsion system performance for different IVR.

where Q^* denotes the dimensionless volumetric flow rate as follows $Q^* = 4Q/V_t\pi D^2$.

Finally, generated thrust and momentum are shown as a function of time in Figure 6.13 and 6.14. Note that both coefficients have been averaged by following eq.6.1 once the curve have reached a periodic state in order to show the results from Table 6.1. On the other hand, in order to decompose the exhibited curves into the frequencies that make it up, the Strouhal number must be defined.

$$St = \frac{fD}{V_t}, \tag{6.2}$$

where f represents the frequency of the signal under consideration.

It is concluded that, even though the amplitude of the curve for the thrust and momentum coefficient becomes slightly greater as Ω increases, the frequency of the curve remains constant regardless of Ω, according to results shown from Figure 6.15 to Figure 6.18, where fast fourier transform (FFT) has been applied in order to convert the original signal to a representation in the frequency domain.

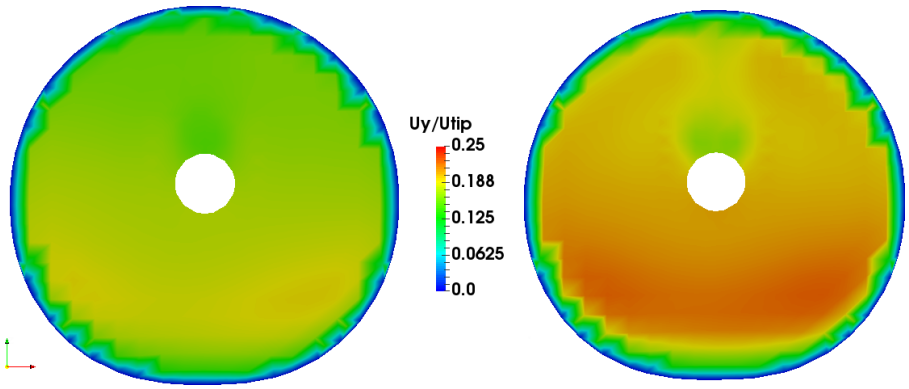

Figure 6.12: Normalized axial velocity at plane just upstream of the impeller; IVR = 1.22 (Left), IVR = 2.49 (Right).

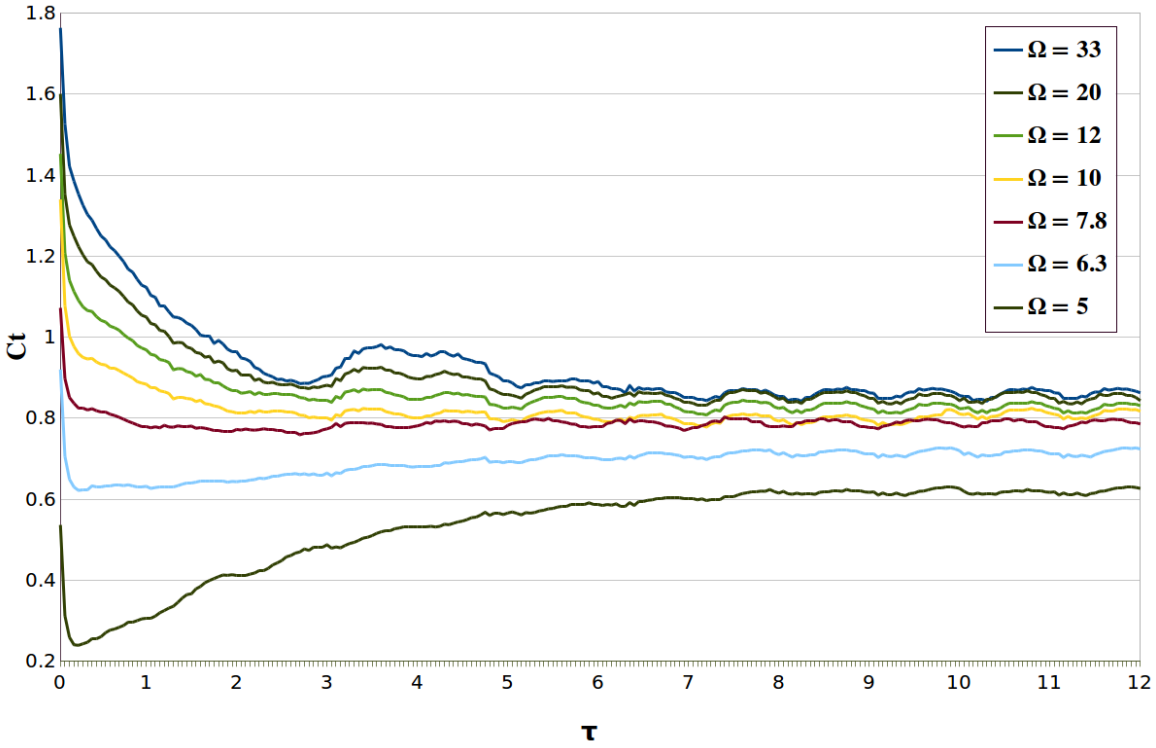

Figure 6.13: Thrust coefficient vs dimensionless time $5 \leq \Omega \leq 33$.

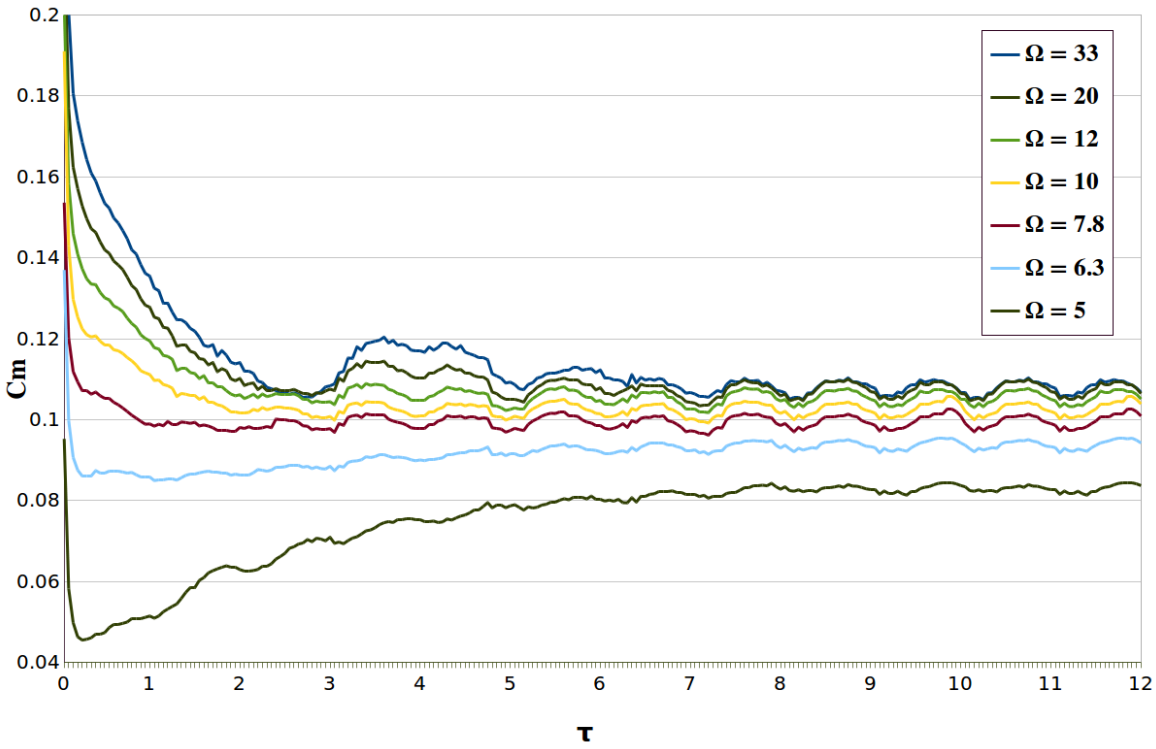

Figure 6.14: Momentum coefficient vs dimensionless time $5 \leq \Omega \leq 33$.

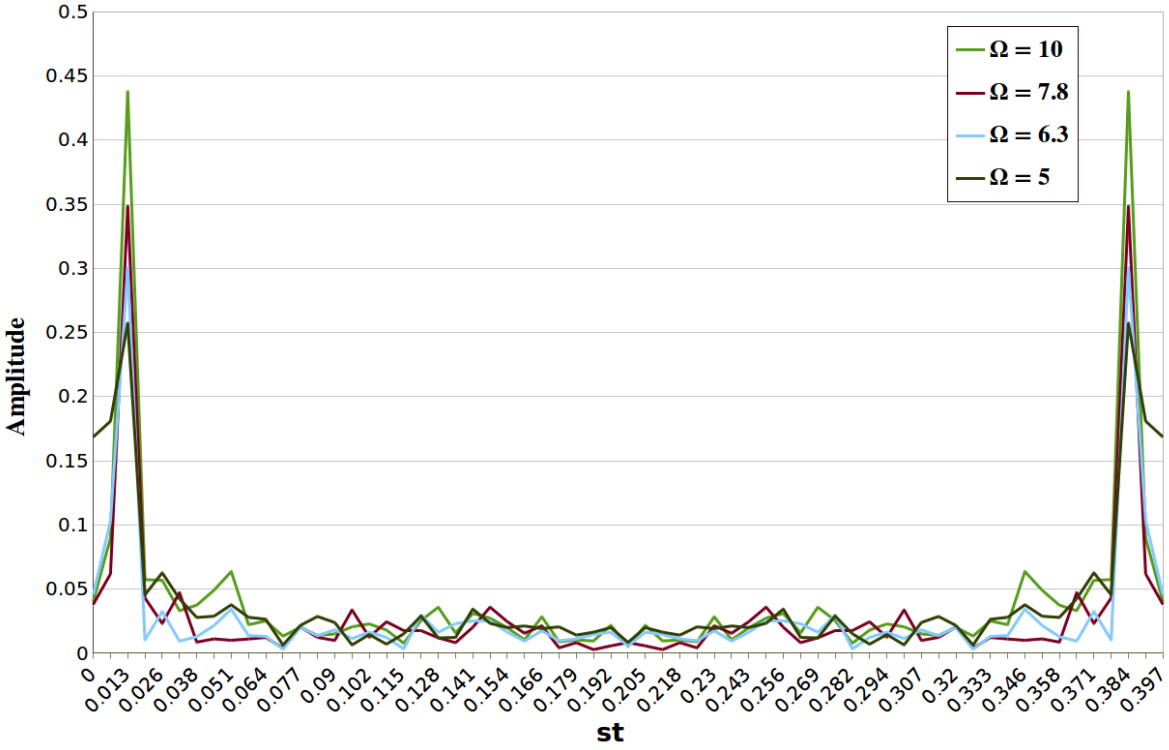

Figure 6.15: Fourier-transform of fluctuating thrust coefficient $5 \leq \Omega \leq 10$.

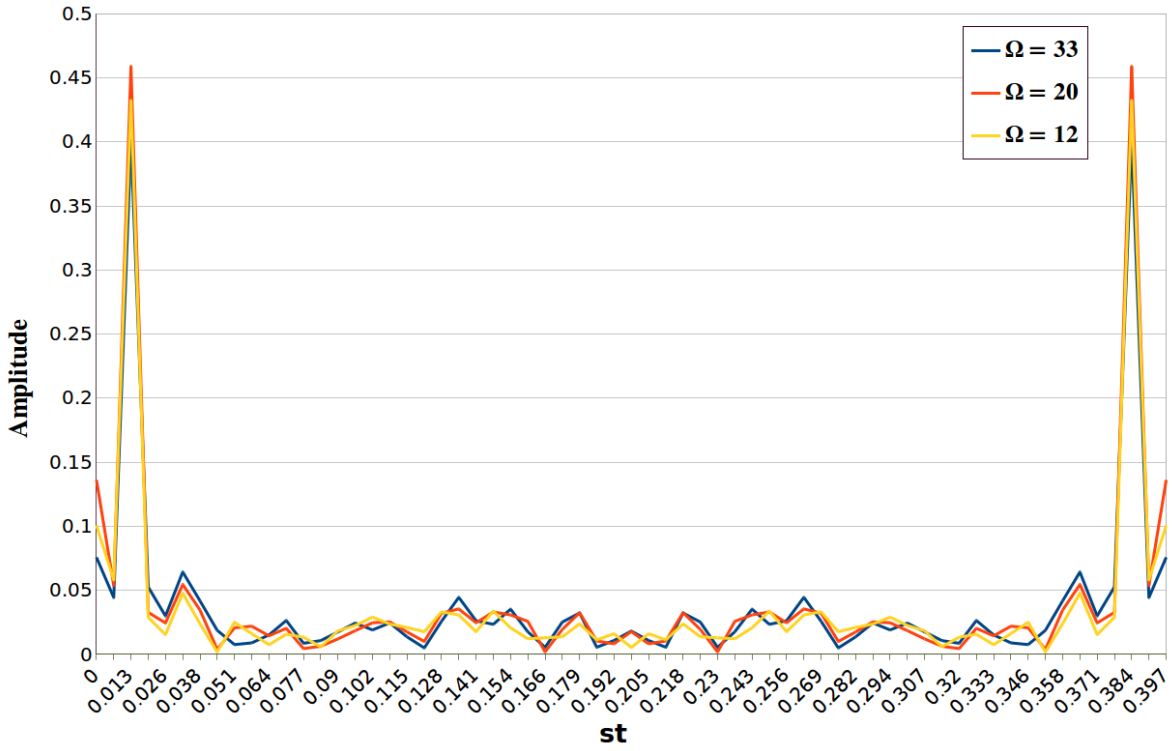

Figure 6.16: Fourier-transform of fluctuating thrust coefficient $12 \leq \Omega \leq 33$.

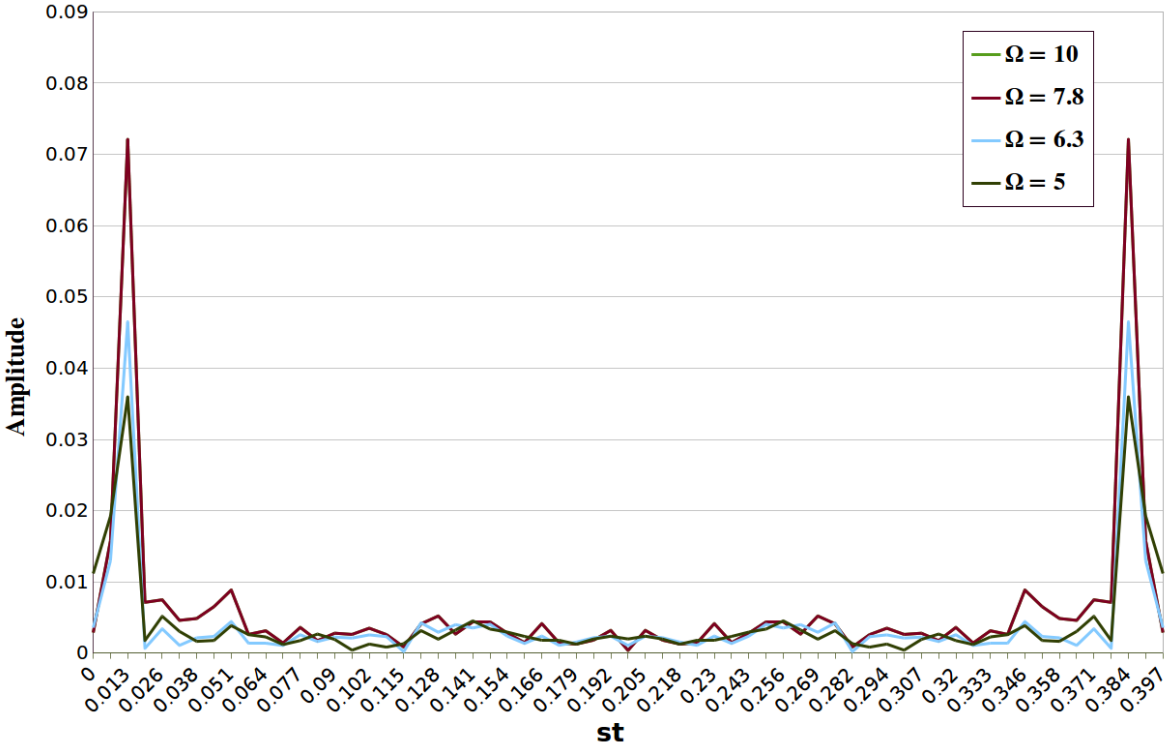

Figure 6.17: Fourier-transform of fluctuating momentun coefficient $5 \leq \Omega \leq 10$.

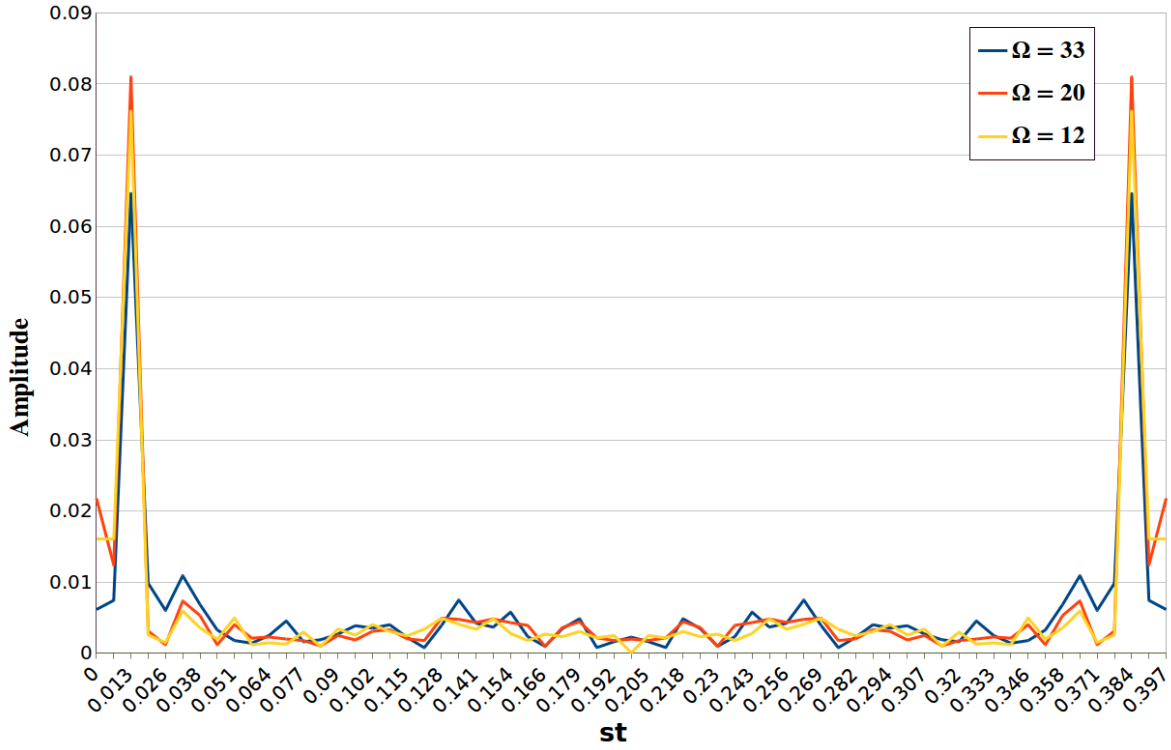

Figure 6.18: Fourier-transform of fluctuating momentun coefficient $12 \leq \Omega \leq 33$.

6.3 Pump exit area analysis

Calculations have been performed for Δ values bounded as follows: $0.77 \leq \Delta \leq 1.28$, maintaining constant the rest of parameters, and searching for improvements on the behavior of the propulsion system within the following range; $\Omega = 10$ to $\Omega = 20$. For this purpose, different operating conditions have been studied for each value of Δ. Figure 6.19 shows changes carried out to the initial geometry Figure 6.20.

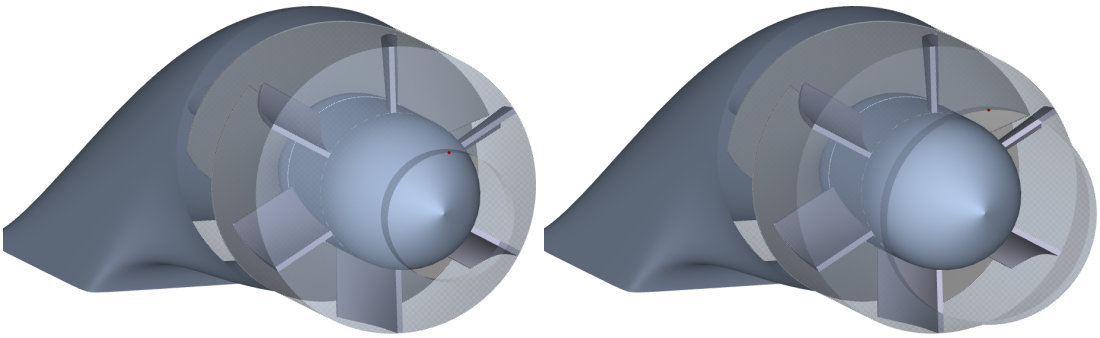

(a) $\Delta = 0.77$ (b) $\Delta = 1.28$

Figure 6.19: Modifications performed over exit area for the initial geometry.

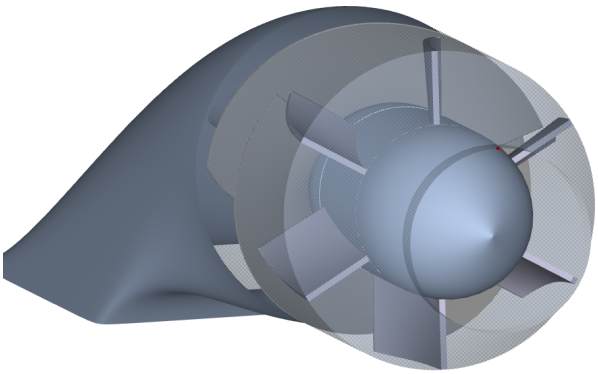

(a) $\Delta = 1$

Figure 6.20: Exit area for the initial geometry.

The results obtained can be observed in Figure 6.21.

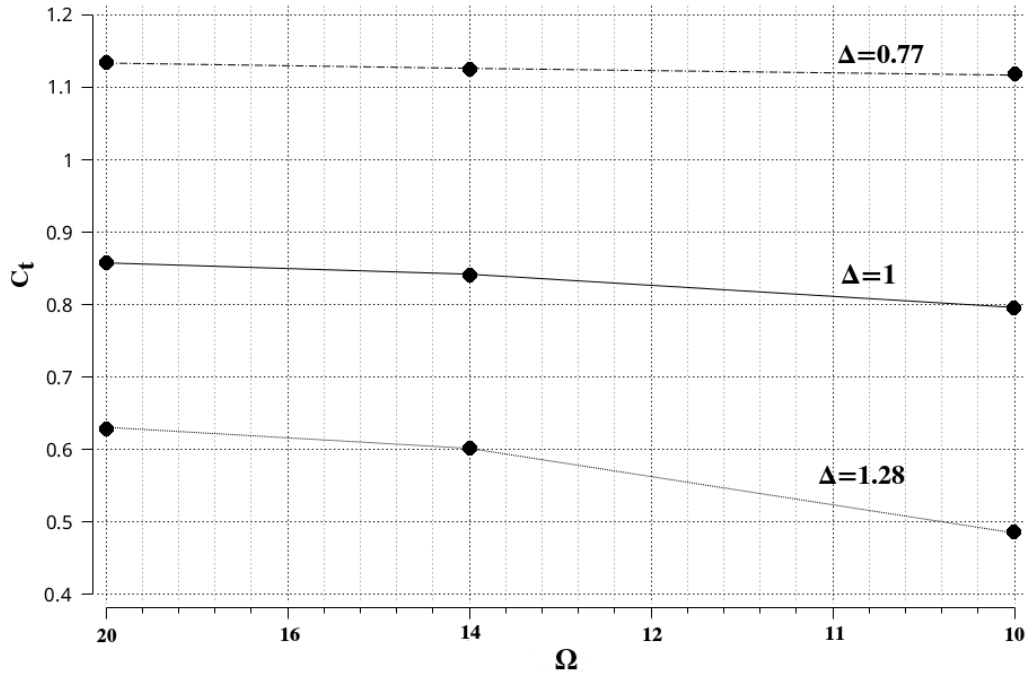

Figure 6.21: Thrust coefficient for different values of Δ at several operating conditions.

where the major improvement has been obtained when a reduction of the exit radio of 23% with regard to the initial geometry is exhibited (Figure 6.19a), achieving a thrust coefficient 31% larger than the same for the initial geometry when $\Omega = 20$. The torque required by the system has been decreased, since the torque require for the impeller, according to the momentum coefficient, has increased 40% (Corresponding to $C_m = 0.14$ in Figure 6.2). So improvements for the thrust generation requires larger expenses on torque generation, since the increasing rate of the last one is larger than the first. Note the thrust coefficient has been enhanced when IVR take values from 0.85 to 1.57 in Figure 6.2 so that the behavior of the propulsion system has been changed to a different range.

Ω	Re_{in}	Δ	IVR	V_p/V_t	Q^*	V_0/V_t	C_m	C_t
20	$5 \cdot 10^6$	0.77	0.85	0.117	0.117	0.347	0.146	1.135
14	$7 \cdot 10^6$	0.77	1.17	0.112	0.119	0.354	0.143	1.127
10	$1 \cdot 10^7$	0.77	1.57	0.127	0.127	0.377	0.141	1.120
20	$5 \cdot 10^6$	1	0.66	0.150	0.150	0.446	0.107	0.859
14	$7 \cdot 10^6$	1	0.89	0.156	0.156	0.463	0.106	0.841
10	$1 \cdot 10^7$	1	1.22	0.164	0.164	0.486	0.102	0.796
20	$5 \cdot 10^6$	1.28	0.57	0.174	0.174	0.516	0.080	0.630
14	$7 \cdot 10^6$	1.28	0.79	0.176	0.176	0.522	0.076	0.604
10	$1 \cdot 10^7$	1.28	1.05	0.190	0.190	0.565	0.064	0.488

Table 6.2: Propulsion system performance for different pump exit radius.

Differences in the pressure coefficient, according to eq 4.13 and considering p_0 at the outlet plane, are shown below (Figure 6.22) for both the initial geometry $\Delta = 1$ and the same when $\Delta = 0.77$.

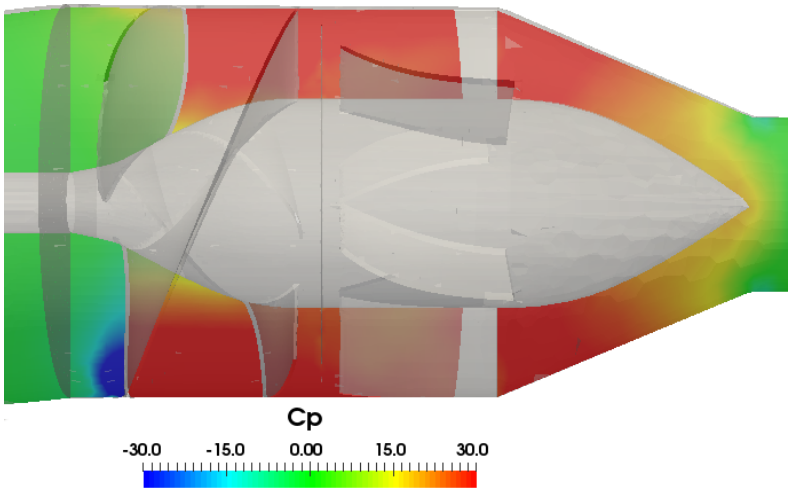

(a) $\Delta = 0.77$

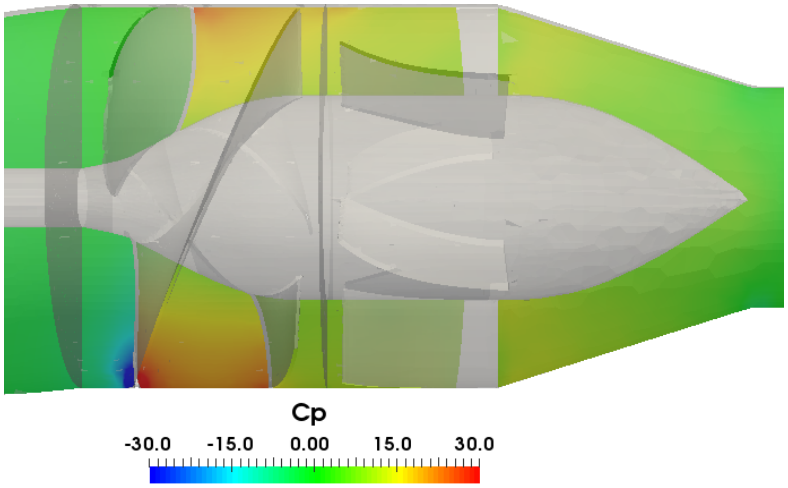

(b) $\Delta = 1$

Figure 6.22: Pressure coefficient for different Δ values.

where it can be observed that bottleneck effect generated in Figure 6.22a has a positive effect over the general performance of the system. On the other hand, the fluid when the exit radio is larger is not held back enough so that pressure losses have a negative effect on the overall performance of the jet-pump for the given operating conditions.

According to results previously shown, changes in the initial geometry could be performed if the desired behavior for the propulsion system is to be changed.

6.4 Trailing Edge pitch analysis

In this part, a similar analysis to the previous section will be carried out. So, maintaining the whole set of design variables constant for the initial geometry, the trailing edge pitch ϕ will be varied from 19º to 28º progressively, keeping constant the same for the leading edge. Changes to the initial geometry can be observed in Figure 6.23

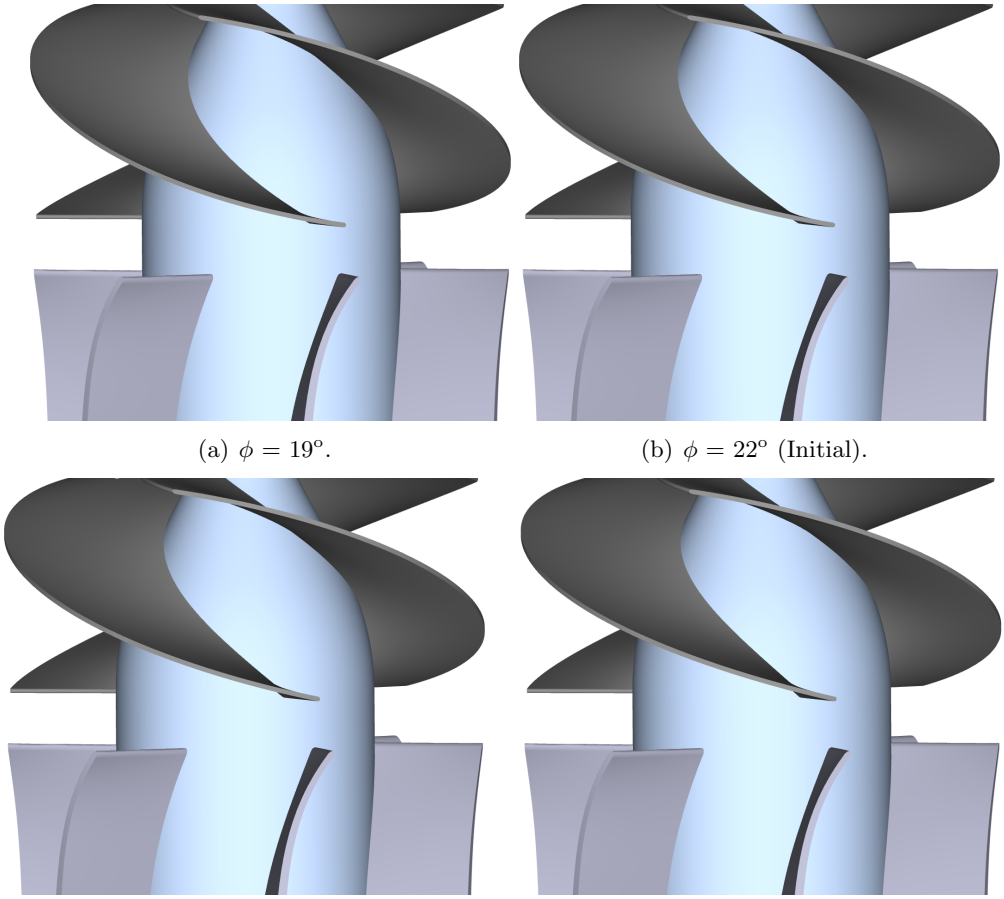

(a) $\phi = 19^{o}$. (b) $\phi = 22^{o}$ (Initial).

(c) $\phi = 26^{o}$. (d) $\phi = 28^{o}$.

Figure 6.23: Modifications performed over trailing edge pitch for the initial geometry .

The results obtained can be observed in Figure 6.24.

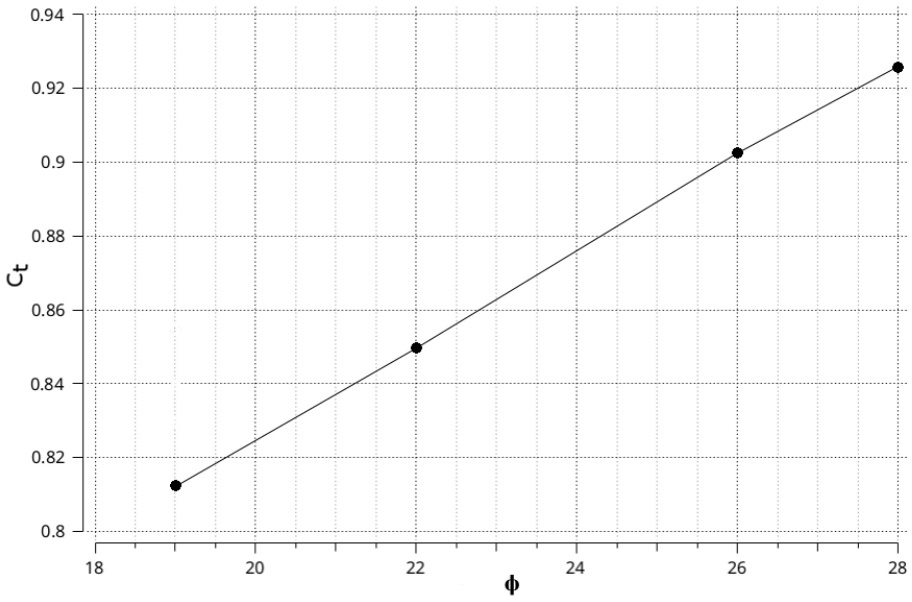

Figure 6.24: Thrust coefficient for several trailing edge pitch values.

The graph representing the thrust coefficient behaves as expected, changes in the trailing edge pitch enhances the thrust generated by the system. Larger values for the trailing edge pitch lead to increments of the blade curvature and enhancements over the blade lift obtained occur. However, this case should be analyzed carefully for several operating conditions since values for the TE pitch too large may influence negatively over the overall performance of the system.

7 Conclusions and future work

The present work was carried out with the intention of deeper understanding the behavior of the jet-pump under study at different operating conditions as well as its overall performance. For this purpose, a CFD analysis with OpenFOAM® was performed. The results obtained for the flow pattern address the importance of the stagnation point to deduce the performance of the system, which increases for lower values of the IVR at constant angular velocity of the impeller, moving the stagnation point towards the duct lip and *vice versa*. On the other hand, pressure coefficient fluctuations were analyzed along the center line of the duct, exhibiting its respective values on the plane just upstream of the impeller, which increased as the IVR index was also increased, decelerating the flow field on its way into the gullet. This effect, allowed us to explain the different values for the thrust coefficient obtained when varying the IVR index, becoming lower when the IVR was increased. The increasing pressure coefficient at the plane just upstream of the impeller reduces the pressure difference between the blade face and the blade back for a constant angular velocity of the impeller.

On the other hand, variations in the pump exit area and increments to the trailing edge pitch have suggested new possibilities for the initial geometry that might enhance the required thrust for a given condition, in spite of the increments in the required torque for the impeller. It has been shown how impeller performance is strongly linked to the pump exit area, where larger values for the thrust coefficient were obtained when the exit area was reduced at a constant angular velocity of the impeller and lower ship velocities. However, there are other parameters that make up the jet-pump that might also exhibit certain influence on the overall performance, i.e., gullet volumetric area, stator blade area and angle of trajectory, venturi rate of compression, venturi "bowl" area and so on, whose analysis requires extensive computational resources since different operating conditions must be applied to each design variable. So a parameterized analysis is proposed in order to asses the impact of the main design variables, defined at the introduction of the present work, over the general jet-pump performance. Multi-phase studies considering the formation of vapor cavities should also be performed so as to analyze the cavitation phenomena, studying its influence over the delivered thrust and the damages caused on the blade surfaces.

Appendix

A OpenFOAM® case review

Three main directories compose the OpenFOAM® case: 0, constant and system. The first stores the initial conditions for the fields. The second stores the mesh, including spatial and connectivity related data. The last stores settings related to numerics and general execution of the simulation. Text files or dictionaries containing such information are stored within each directory. Figure A.1 shows an scheme of the case directory.

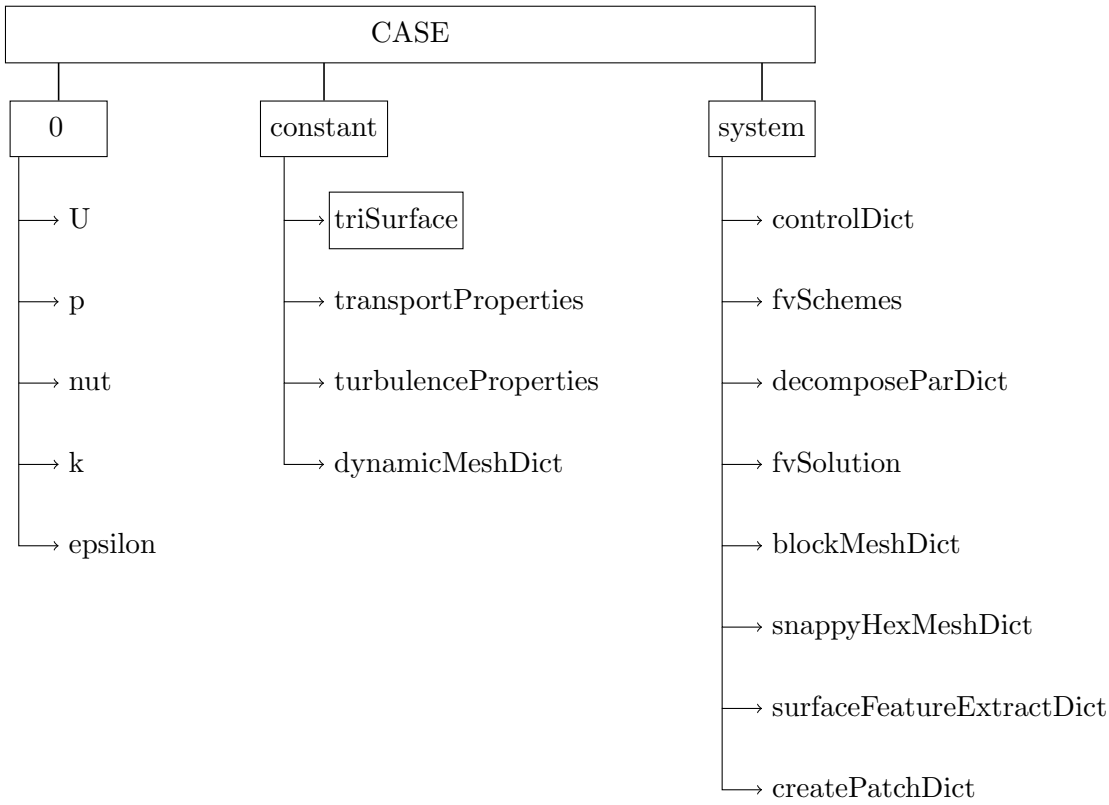

Figure A.1: OpenFOAM® case scheme.

Meshing procedure in OpenFOAM®

Firstly, the STL files generated by CAESES containing the geometric model are stored within the constant/Surface folder. Input parameters, required for the meshing process by `blockMesh` and `snappyHexMesh` can be found within `blockMeshDict`, `surfaceFeatureExtractDict` and `snappyHexMeshDict` dictionaries. Once these applications are run, the computational grid is generated and stored within the constant/polymesh directory, which is automatically created for this purpose subsequently.

The execution of `snappyHexMesh` can be split into two mayor steps. Firstly, the geometry within the triSurface directory is automatically read and added to the existing background mesh. The cells near the wall surface are refined according to the specifications given below. Then, the cells that are not inside the flow domain are removed. This is usually known as the `castellatedMesh` process. Secondly, mesh points in the vicinity of the surface are adjusted and moved onto the surface by means of the `snap` procedure. There is a third available procedure which is aimed to add extra cells near the wall so as to refine the mesh in that region, but it will not be discussed in the present work.

The required parameters to run `snappyHexMesh` are defined within `snappyHexMeshDict`. The refinementSurface level specifies the minimum and maximum level of refinement. The minimum is applied generally over the surface while the maximum is only applied to those cells that run into intersections forming an angle greater than 30^{o} (specified by `resolveFeatureAngle`) and so to surfaces of greater curvature. The feature level corresponds to the specific refinement level for those selected edges within the geometry and extracted from the `surfaceFeatureExtract` utility. This edges selection is made according to the following rule (Table A.10) for every geometry file except for those categorized as *null*. in which all of the edges whose adjacent surface normals are at an angle less than 150 degrees are selected to be refined (edges belonging to surfaces of greater curvature).

Boundary conditions, fluid properties, turbulence model in OpenFOAM®

Once the `polymesh` directory has been generated, the boundary file contains all of the information concerning to mesh boundaries or boundary-patches. Then, according to these boundary-patches, boundary conditions are defined within the `0` time step directory as well as the initial state of the fields involved in the simulation, which in this case are `U`, `p`, `nut`, `k` and `epsilon`.

In this part, an overview is provided on how the fields are set before the start of the simulation. For this purpose, initial and boundary conditions are required to be defined. That is, initial internal field values as well as boundary field values (values at mesh boundaries) need to be established. However, in order to define the boundary conditions, the boundary type of the domain or mesh boundaries are to be previously specified. Mesh boundaries are usually referred as boundary-patches. There are several patch types that can be assigned to a mesh boundary. An outline of the patch types applied to every surface is given in table A.1.

name	type	inGroups
Tunnel	wall	wall
DriveShaft	wall	wall
Gullet	wall	wall
Impeller	wall	wall
Shroud	wall	wall
Stator	wall	wall
Cone	wall	wall
Venturi	wall	wall
inlet	patch	
outlet	patch	
outlet2	patch	
AMI1	cyclicAMI	cyclicAMI
AMI2	cyclicAMI	cyclicAMI

Table A.1: Scheme of boundaries patches applied.

where applied boundary patches are explained below.

- **patch**: Any boundary condition of Neumann, Dirichlet or Cauchy can be applied to boundary patches of this type.
- **wall**: It enables the turbulence models to apply the wall functions to that boundary. This boundary path does not imply that there is no flow through the boundary, which must be explicitly defined via the velocity boundary condition.
- **cyclicAMI**: Arbitrary Mesh Interface (AMI) technique allows the transient simulation of adjacent mesh domains that move relative to each other. It enables two patches to be treated as if they are physically connected. The cyclicAMI boundary condition has been used for those sliding interfaces that separate the rotating mesh region around the impeller from those remaining still.

Additionally, in order to apply the last boundary path type to both interfaces separating the rotating mesh from the rest of the domain, the tool `createPatch` implemented with OpenFOAM is used, whose required input parameters are stored within the `createPathDict` dictionary (Table A.2). An auxiliary geometry under the name ShroudInter has been generated for this purpose.

```
patches
        name                AMI1;
        patchInfo
            type            cyclicAMI;
            matchTolerance  0.0001;
            neighbourPatch  AMI2;
            transform       noOrdering;
        constructFrom patches;
        patches (ShroudInter);

        name                AMI2;
        patchInfo
            type            cyclicAMI;
            matchTolerance  0.0001;
            neighbourPatch  AMI1;
            transform       noOrdering;
        constructFrom patches;
        patches (ShroudInter_slave);
```

Table A.2: createPatchDict.

ShroudInter_slave will remain still while ShroudInter moves in conjunction with the region that contains the impeller.

Once mesh boundary types have been specified, initial and boundary conditions for the field can be set. An outline of the definition of these conditions can be found in Table A.3

and Table A.4.

Subdictionary		U Entries	P Entries
dimensions		[0 1 -1 0 0 0 0]	[0 0 -2 -2 0 0 0]
internalField	uniform	(0 0 0)	0
boundaryField			
inlet			
	type	fixedValue	zeroGradient
	value	uniform (0 1 0)	
outlet			
	type	inletOutlet	fixedValue
	value	uniform (0 0 0)	uniform 0
	inletValue	uniform (0 0 0)	
outlet2			
	type	inletOutlet	fixedValue
	value	uniform (0 0 0)	uniform 0
	inletValue	uniform (0 0 0)	
wall			
	type	noSlip	zeroGradient
Tunnel			
	type	Slip	
DriveShaft			
	type	Slip	
Impeller			
	type	movingWallVelocity	
	value	uniform (0 0 0)	
Impellerblade			
	type	movingWallVelocity	
	value	uniform (0 0 0)	

Table A.3: Outline of U and p dictionaries.

where *dimensions* refers to dimension orders in the following units (kilogram, meter, second, Kelvin, mole, Ampere, Candela). So the pressure refers to the kinematic pressure. The next, internalField, defines initial conditions for the internal field. Then, boundaryField specifies boundary conditions for each patch previously defined in Table A.1. Note that wall entry consist of the inGroup `wall`.

Subdictionary		K Entries	epsilon Entries	nut Entries
dimensions		[0 2 -2 0 0 0 0]	[0 2 -3 0 0 0 0]	[0 2 -1 0 0 0 0]
internalField	uniform	0.06	0.0495	0
boundaryField				
inlet				
	type	fixedValue	fixedValue	calculated
	value	$internalField	$internalField	uniform 0
outlet				
	type	inletOutlet	inletoutlet	calculated
	value	$internalField	$internalField	uniform 0
	inletValue	$internalField	$internalField	
outlet2				
	type	inletOutlet	inletoutlet	calculated
	value	$internalField	$internalField	uniform 0
	inletValue	$internalField	$internalField	
wall				
	type	kqRWallFunction	epsilonWallFunction	nutkWallFunction
	value	$internalField	$internalField	uniform 0

Table A.4: Outline of k,epsilon and nut dictionaries.

Information related to fluid properties, turbulence model and type of motion for the impeller is stored within the following dictionaries respectively; `transportProperties`, `turbulenceProperties`, `dynamicMeshDict`. An outline of the entries for the previous dictionaries is shown in Table A.5, A.6 and A.7.

transportModel	Newtonian;	
nu	[0 2 -1 0 0 0 0]	1e-6;

Table A.5: Dictionary entries for transportProperties.

simulationType	RAS;	
RAS		
	RASModel	kEpsilon;
	turbulence	on;

Table A.6: Dictionary entries for turbulenceProperties.

dynamicFvMesh	solidBodyMotionFvMesh;	
motionSolverLibs	("libfvMotionSolvers.so");	
solidBodyMotionFvMeshCoeffs		
	cellZone	ShroudInter;
	solidBodyMotionFunction	rotatingMotion;
	rotatingMotionCoeffs	
	origin	(0 0 0);
	axis	(0 1 0);
	omega	100;

Table A.7: Dictionary entries for dynamicMeshDict.

Subdictionary		Entries		
castellatedMesh	true;			
snap	true;			
addLayers	false;			
geometry				
	type	name	regions	region name
Tunnel.stl	triSurfaceMesh	Tunnel	ColorWall	Tunnel
			ColorIntlet	inlet
			ColorOutlet2	outlet2
DriveShaft.stl	triSurfaceMesh	DriveShaft	ColorWall	DriveShaft
Gullet.stl	triSurfaceMesh	Gullet	ColorWall	Gullet
Impeller.stl	triSurfaceMesh	Impeller	ColorWall	Impeller
			Colorimpblade	Impellerblade
Shroud.stl	triSurfaceMesh	Shroud	ColorWall	Shroud
ShroudInter.stl	triSurfaceMesh	ShroudInter	ColorInter	ShroudInter
Stator.stl	triSurfaceMesh	Stator	ColorWall	Stator
			Colorvanblade	Statorblade
Cone.stl	triSurfaceMesh	Cone	ColorWall	Cone
Venturi.stl	triSurfaceMesh	Venturi	ColorWall	Venturi
			ColorOutlet	outlet
castellatedMeshControls				
features				
	file	level		
	Tunnel.eMesh	0		
	DriveShaft.eMesh	1		
	Gullet.eMesh	1		
	Impeller.eMesh	3		
	Shroud.eMesh	1		
	Stator.eMesh	3		
	Venturi.eMesh	1		
refinementSurfaces				
	file	level		
	Tunnel	(0 0)		
	DriveShaft	(1 2)		
	Gullet	(1 2)		
	Impeller	(2 3)		
	Impeller_Blades	(3 3)		
	Shroud	(2 2)		
	Stator	(3 3)		
	Stator_Vanes	(3 3)		
	Cone	(2 2)		
	Venturi	(1 2)		
	ShroudInter	(1 2)		
	faceType	boundary;		
	cellZone	ShroudInter;		
	faceZone	ShroudInter;		
	cellZoneInside	inside;		
resolveFeatureAngle 30;				
locationInMesh (0.01 -0.1 0.04);				

Table A.8: Scheme of main imput parameters for `snappyHexMeshDict`.

Subdictionary	Terms	Entries
numberOfSubdomains		4
method		hierarchical
hierarchicalCoeffs	n	(1 1 4)
	delta	0.001
	order	xyz

Table A.9: Dictionary entries for decomposeParDict.

geometryfile.stl	
extractionMethod	extractFromSurface;
extractFromSurfaceCoeffs	
includedAngle	150;

Table A.10: Dictionary entries for surfaceFeatureExtract.

Simulation setup in OpenFOAM®

Before running the simulation, the dictionary `decomposeParDict` (Table A.9) must be defined in order to run the solver pimpleDyMFoam in parallel on distributed processors and so speeding up the simulation time.

The mesh and fields are decomposed into 4 processors. The utilized method is known as hierarchical domain, in which the domain is split geometrically into 4 sub-domains following the subsequent order xyz, where delta is the cell skew factor. Several tests have been carried out in order to choose the current hierarchical order for the domain decomposition. This arrangement resulted the fastest in the face of later computations.

Whithin the `controlDict` dictionary, essential input parameters for running the simulation are set. The keyword entries are listed in table A.11.

The `fvSchemes` dictionary sets finite volume discretization schemes for all of the terms that are calculated during a simulation. OpenFOAM® includes a vast number of discretisation schemes, but only the shemes used in the present work are summarized into the table below (Table A.12). However, the explanation of the subsequently shown discretization schemes is beyond the scope of this analysis (see (Maric et al., 2014), (Ferziger and Perić, 2002) and (Foundation, 2016) for a more in detail review of this topic). If a default scheme is specified within a particular subdictionary, that precisely scheme is assigned to all of the terms to which the subdictionary refers except for those precise terms whose scheme is specified and so override the default scheme.

The `fvSolution` dictionary sets the equation solvers, tolerances and algorithms. The first subdictionary (solvers) specifies each linear-solver that is used for each discretized equation. The PIMPLE subdictionary controls the looping of the entire set of governing equations when running the solver `pimpleDyMeshFoam`. The succeeding subdictionary (relaxationFactors) consist of a technique used for improving stability of the computation by limiting the amount which a variable changes from one iteration to the next)

Subdictionary		Entries
application		pimpleDyMFoam;
startFrom		startTime;
startTime		0;
stopAt		endTime;
endTime		0.18;
deltaT		0.000001;
writeControl		adjustableRunTime;
writeInterval		0.005;
purgeWrite		0;
writeFormat		binary;
writePrecision		6;
writeCompression		off;
timeFormat		general;
timePrecision		6;
runTimeModifiable		true;
adjustTimeStep		yes;
maxCo		0.5;
functions		
forces	type	forces;
	libs	(”libforces.so”);
	writeControl	timeStep;
	timeInterval	1;
	log	yes;
	patches	(Impellerblade);
	rho	rhoInf;
	log	true;
	rhoInf	1000;
	CofR	(0 0 0);
	pitchAxis	(0 1 0);
	magUInf	1;
	lRef	1;
	Aref	0.7854;
flowRatePatch		
	name	outlet;

Table A.11: controlDict.

Subdictionary	Refers to	Discretization Scheme Entries
ddtScheme	First time derivative $\partial/\partial t$	default Euler
d2dt2Scheme	Second time derivative $\partial^2/\partial^2 t$	default Euler
gradSchemes	Gradient ∇	default Gauss linear grad(p) Gauss linear grad(U) cellLimited Gauss linear 1
divSchemes	Divergence $\nabla\cdot$	default none div(phi,U) Gauss linearUpwind grad(U) div(phi,k) Gauss upwind div(phi,epsilon) Gauss upwind div((nuEff*dev2(T(grad(U))))) Gauss linear
laplacianSchemes	Laplacian ∇^2	default Gauss linear limited corrected 0.33
interpolation Schemes	cell to face interpolations of values	default linear
snGradSchemes	component of gradient normal to a cell face	limited corrected 0.33

Table A.12: fvSchemes.

Subdictionary	Terms	Entries
Solvers	pcorr	solver GAMG
		tolerance 1e-2
		relTol 0
		smoother DICGaussSeidel
		cacheAgglomeration no
		maxIter 50
	p	$pcorr
		tolerance 1e-5
		relTol 0.01
	pFinal	$p
		tolerance 1e-6
		relTol 0
	"(U|k|epsilon)"	solver smoothSolver
		smoother symGaussSeidel
		tolerance 1e-6
		relTol 0.1
	"(U|k|epsilon)Final"	solver smoothSolver
		smoother symGaussSeidel
		tolerance 1e-6
		relTol 0
PIMPLE		correctPhi no
		nOuterCorrectors 2
		nCorrectors 1
		nNonOrthogonalCorrectors 0
relaxationFactors		"(U|k|epsilon).*" 1

Table A.13: fvSolution.

B Sea-Doo xp 951 99 parts

In order to identify the problem under study properly, the whole propulsion system on which this analysis is based on is shown below. The impeller can be observed in figure B.1. The jet pump housing, also known as stator and so their vanes can be observed in Figure B.2. Both parts constitute the main elements of the propulsion system in conjunction with the impeller drive shaft, the intake housing or gullet (both represented in Figure B.3) and the rear venturi (Figure B.4), which is shown next to the steering nozzle, even though the last is not modeled (see considered assumptions in section 4.2).

(a) Impeller side elevation. (b) Impeller plan view.

Figure B.1: Stainless steel impeller with progressive pitch 16º-19º Ref.271000810.

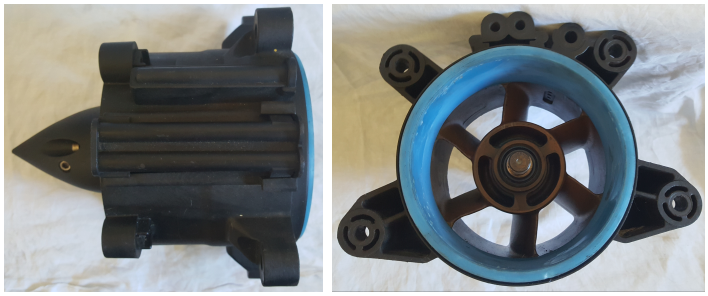

(a) Housing side elevation. (b) Housing front elevation.

Figure B.2: Sea-Doo xp 951 99 jet-pump housing or stator.

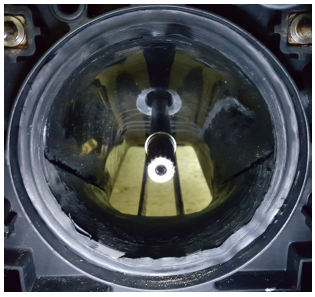

Figure B.3: Sea-Doo xp 951 99 gullet and drive shaft.

Figure B.4: Sea-Doo xp 951 99 venturi and nozzle.

C Domain measures

The most significant lengths of the domain are shown in the table below (Table C.1).

Part	Measure	n
Impeller	Impeller Diameter (D)	1
	Hub Tip Diameter	0.16
	Hub Base Diameter	0.27
	Hub Height	0.58
	LE Root vertical distance from Hub Tip	0.1
	LE Tip vertical distance from Hub Tip	0.2
	LE Pitch Torsion from Root	5º
	LE Pitch Angle	16º
	TE vertical distance from Hub Tip	0.56
	TE Pitch Torsion from Root	5º
	TE Pitch Angle	25º
	Blade thickness	0.013
Jet Pump Housing	Housing (Shroud) and Vanes Diameter	1
	Hub Diameter	0.27
	Hub Height	0.45
	LE vertical distance from Housing Hub Tip	0.05
	TE vertical distance from Housing Hub Tip	0.45
	LE Pitch Angle	30º
	TE Pitch Angle	0º
	Rear Cone Hight	0.67
	TE vertical distance from Housing Hub Tip	0.45
Others	Venturi Outlet Diameter	0.58
	Drive Shaft Length	1.62
	Drive Shaft Diameter	0.16
	Gullet Inlet Length	1.5
	Gullet Inlet Width	1
	Total Domain Length	4.8
	Total Domain Width	1

Table C.1: Measures obtained from real parts under study.

where D is the impeller diameter, which represents the overall width of the impeller from blade tip to blade tip. The rest of the measures are exhibited as n times the impeller diameter, except for those representing angles.

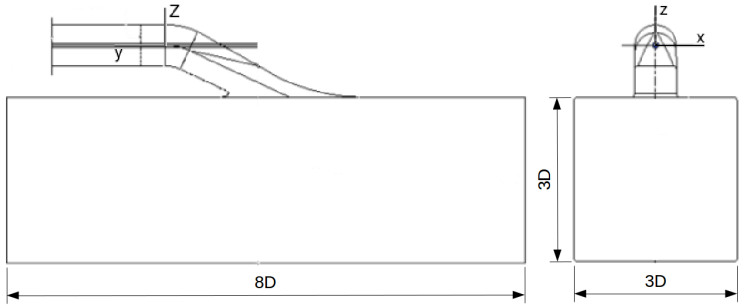

Figure C.1: Sketch of the intake tunnel dimensions and reference coordinate system.

D CAESES software and geometric modeling

CAESES is a software platform which allows the generation of complex 3D surfaces. It has been offering a free version until December 2016. However, a free non-commercial academic license of the power edition for free can be obtained.

Basically, the election of this software stems from the following features:

- It is a powerful 3D modeler, specially designed to generate robust flow-exposed geometries. Comparing to other traditional tools, which are detailed-oriented, CAESES does not encompass any features which may not be relevant for the simulation.
- On the other hand, parametric controls that preserve the robustness of the geometry are included.
- Moreover, CAESES can launch, control and integrate openFOAM®. Even though the simulation setup is carried out as traditionally, modifying the dictionaries within the case directory, the integration of openFOAM® permits to automate the process in which the geometry is exported, meshed, pre-processed and integrated within the CFD code for the simulation. It allows you to save when solving all of the variants that arise when changes on the initial geometry or mesh are applied.
- CAESES also works with the STL format, suitable for the succeeding meshing tool.

Additional information about the characteristics of this software can be found here (CAESES, 2017).

Below it is summarized the process in which the geometry is modeled. However, since it constitutes a tedious procedure and basic knowledge of the presented software are required, a general description of the modeling is carried out so that it can be performed on other CAD tools.

<table>
<tr><td colspan="2">Impeller</td></tr>
<tr><td>Explanation</td><td>Stage</td></tr>
<tr><td>

- Coordinates measured from local reference system on the Hub Tip.
- Hub, Shroud, LE and TE curves definition shown on the right.
- Hub from surface of revolution based on third degree spline composed of 5 points: (0.08D,0,0), (0.1D,0,0.11D), (0.2D,0,0.31D),(0.27D,0,0.47D), (0.27D,0,0.58D).
- Camber curve definition: Start and end points (0° to 180°), LE Pitch (16°), TE Pitch (parameterized), Pitch at root (29°).

</td><td> 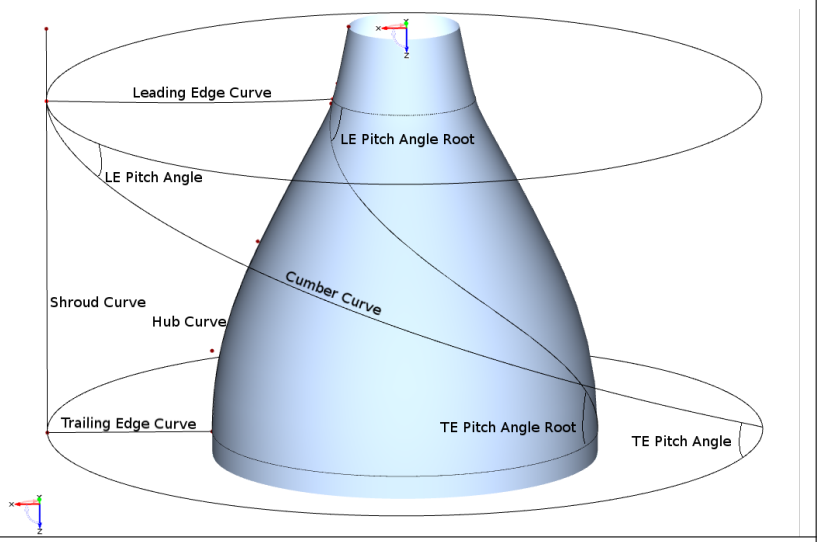
</td></tr>
<tr><td>

- Camber surface definition based on camber curve path: variation of Pitch from root to tip approached by first degree polynomial
- Rake Angle at 10° added by modifying initial LE curve: spline perpendicular to hub axis.

</td><td> 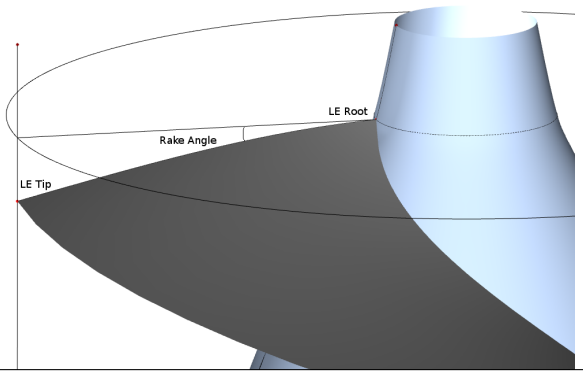
</td></tr>
<tr><td>

- Skew angle added, 45° measured at LE tip.
- Skew angle stems from a spline curve which is at 0° at the LE root with regard to the x axis and at 45° at the LE tip with regard to the shroud tangent

</td><td> 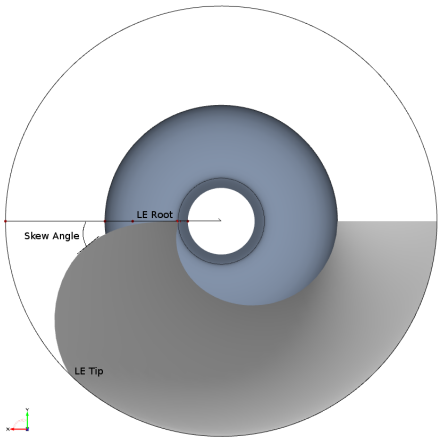
</td></tr>
</table>

Table D.1: Geometry generation steps Part 1.

• Blade solid created from boolean operation: hub, shroud, and offsets on camber surface (blade thickness 0.012D). • Ellipse factor 3 added at the LE and 2 for the TE. • Blade solid is repeated 3 times symmetrically with regard to z axis.	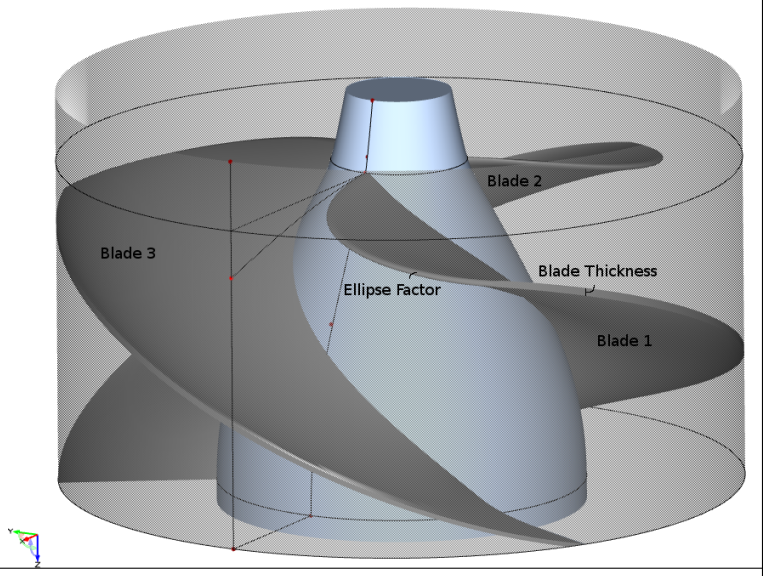
Stator	
• Vane Camber Surface defition based on camber curve path: constant AOA from LE root to LE tip at 25 degrees • TE AOA constant at 0º • LE perpendicular displacement 0.11D	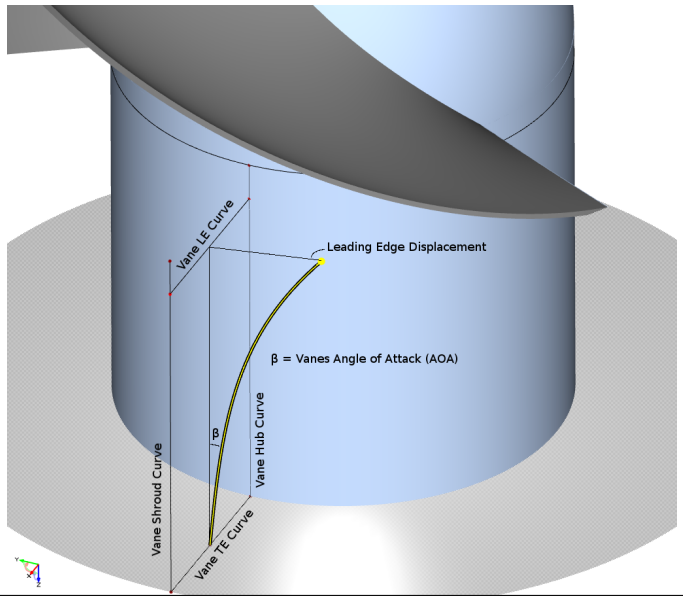
• Vane solid created from boolean operation: Vane hub, shroud, Vane TE surface of revolution and offsets on Vane camber surface (blade thickness 0.013D). • Vane Ellipse Factor 2 at LE • Vane solid is repeated 6 times symmetrically with regard to z axis.	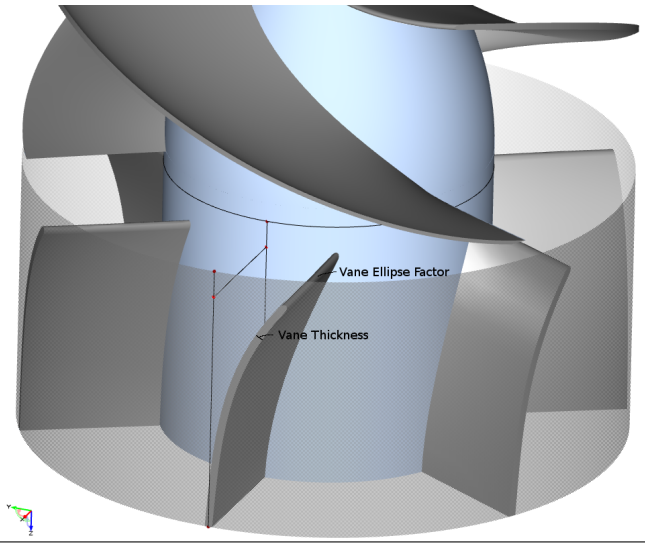

Table D.2: Geometry generation steps Part 2.

<table>
<tr><td colspan="2">Cone Rear</td></tr>
<tr><td>

- Coordinates measured from local reference system on the Impeller Hub Tip (first Figure Table D.1)
- A third order spline approaches all of the points of the real cone
- The cone consists of a surface of revolution based on the previous spline.

</td><td> 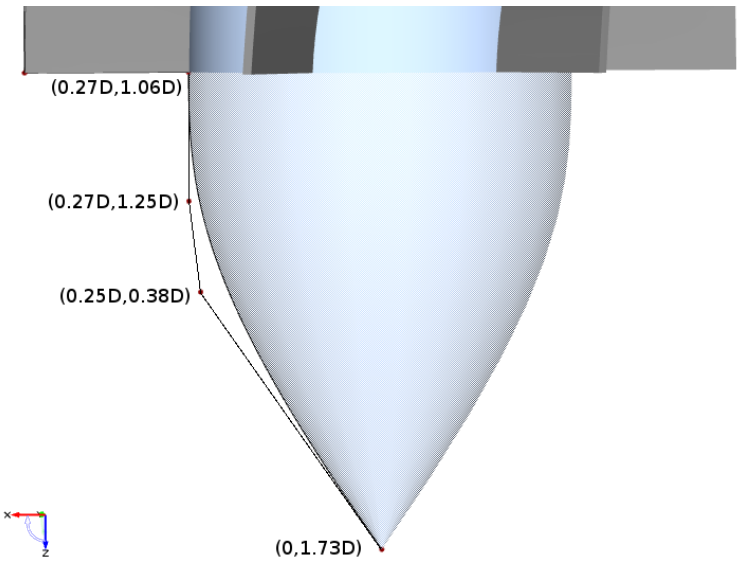
</td></tr>
<tr><td colspan="2">Gullet/Shroud/DriveShaft</td></tr>
<tr><td>

- Intake Housing or Gullet surface stems from an extrusion along a path based on profile 1 and 2.
- Values for dx and dz are 0.13D and 1.85D respectively.
- Path based on spline parallel to z-axis at start and including and Intake Angle of 35 degrees.
- DriveShaft through extrusion of Impeller Hub Tip up to the Gullet Surface.
- Shroud based on extension of Gullet.

</td><td> 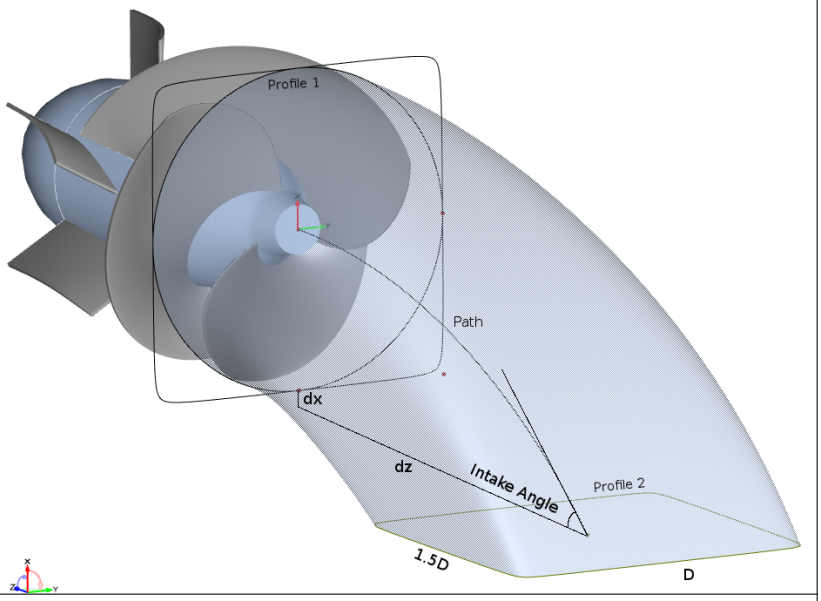
</td></tr>
<tr><td colspan="2">Venturi</td></tr>
<tr><td>

- Venturi generated from surface of revolution considering an outlet diameter of 0.58D and a rear thickness of 0.013D

</td><td> 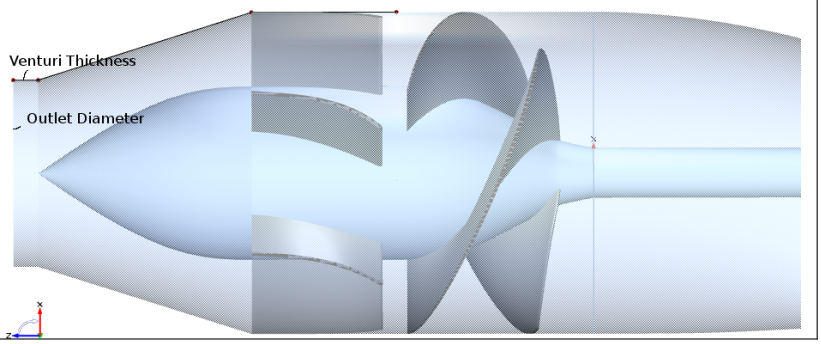
</td></tr>
</table>

Table D.3: Geometry generation steps Part 3.

Jet-Pump Assembly	
• The entire Jet-Pump consists of the assembly of the previously designed parts with a total length of 4.8D and width of D	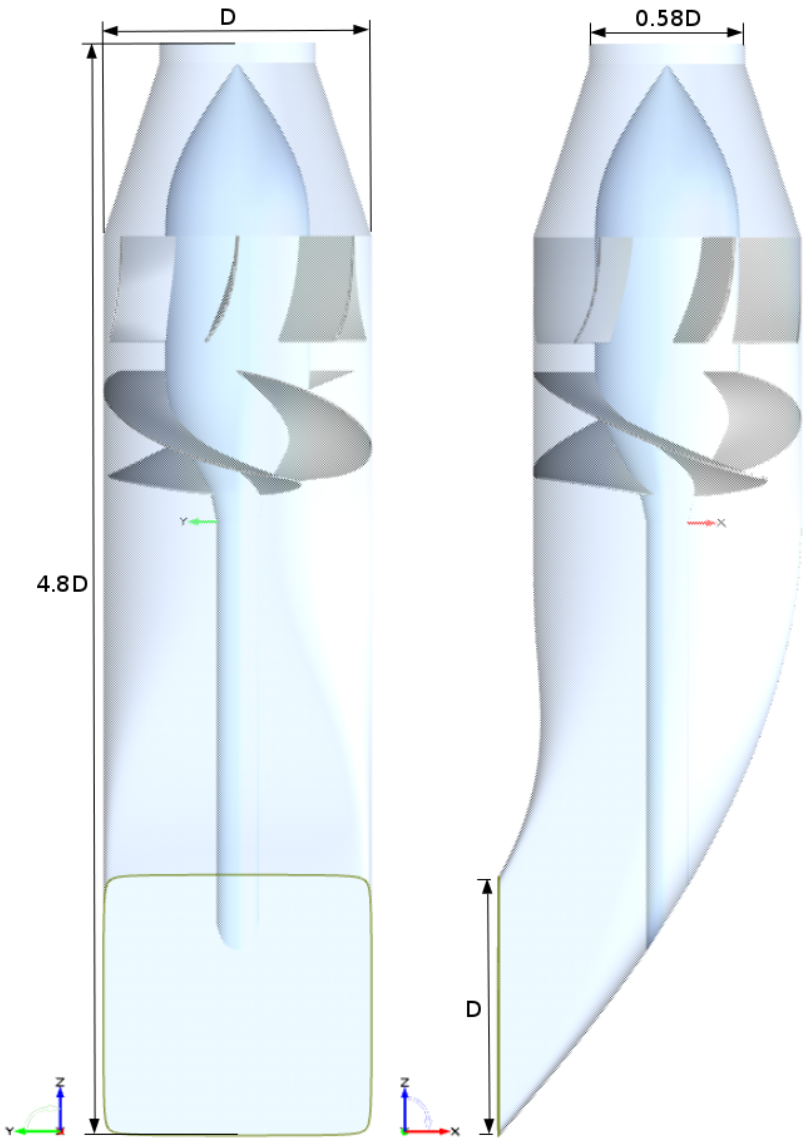

Table D.4: Geometry generation steps Part 4.

E Mesh validation

Convergence and accuracy of the results obtained by a particular simulation depends on so many factors, such as the mathematical model or the numerical scheme used to approximate the solution, and so many setup parameters. Coding errors or code validation, e.g. "solving governing equations right", is not an issue in the present work. Nevertheless, the mesh has a fundamental role on this topic, so a detailed analysis of the mesh quality will be performed, whose resolution will be limited by computational constraints.

According to the previous paragraph, a mesh validation procedure based on Richardson Extrapolation method, also known as "h^2 extrapolation" or "iterated extrapolation", will be performed in order to answer the following questions: how accurate can the representation of the flow domain be constructed without compromising the computational cost ? Where can the complexity of the domain be reduced without impacting the solution accuracy?

A grid refinement study will be performed in order to quantify the uncertainty of grid convergence and so estimating the grid convergence accuracy of our discretized solution. There are other possible techniques for the quantification of numerical uncertainty, but systematic grid refinement studies are the most common and reliable (Roache, 1994).

Basically, the idea is to relate the results from any grid refinement test to the expected results from a grid doubling. This procedure will be developed by the use of a Grid Convergence Index (GCI), which is based upon a grid refinement error estimator. The GCI is derived from the theory of Richardson Extrapolation. It is also important to note that we are concerned with quantifying the discretization errors, which by definition vanish as the grid spacing $h \to 0$ in a hypothetical mesh with infinite number of cells and obtaining a theoretical f_{exact} solution. It is important to note that a significant aspect of Richardson Extrapolation method is that it can also be applied to solution functionals such as force coefficients.

A generalization of Richardson Extrapolation is exhibited below

$$f_{exact} \approx f_1 + \frac{f_1 - f_2}{(r^p - 1)}, \tag{E.1}$$

where $r = h_2/h_1$ is defined as the grid refinement ratio, f_1 and h_1 are the discrete solution and discrete spacing for the fine grid respectively, f_2 and h_2 are the same for coarse grid and p is the numerical method order.

From Eq.(E.1), an error estimator of the fine grid solution , expressed as an Estimated fractional error E_1, is shown below

$$E_1 = (f_1 - f_{exact})/f_1 \approx \frac{\epsilon}{(r^p - 1)}, \tag{E.2}$$

$$\epsilon = (f_2 - f_1)/f_1, \tag{E.3}$$

where E_1 is a good approximation when the solution is of reasonable accuracy, i.e., when $E_1 \ll 1$. The most common use of this method is with a grid doubling $h_2 = 2h_1$ and so $r = 2$. Additionally, for a second order method, where $p = 2$, the equation E.1 can be written as follows

$$f_{exact} \approx \frac{4}{3} f_1 - \frac{1}{3} f_2, \tag{E.4}$$

The idea of the GCI is to relate the ϵ obtained by whatever grid refinement study to the ϵ that would be expected from a grid refinement study of the same problem with the same fine grid using a grid doubling ($r = 2$) with a second-order method ($p = 2$), making the use of grid doubling with second-order method the standard for comparison. So the GCI will be the absolute value of $\epsilon_{equivalent}$ that would produce the same E_1 with $p = 2$ and $r = 2$. This is conveniently expressed as

$$\text{GCI} = 3|\epsilon|/(r^p - 1). \tag{E.5}$$

On the other hand, if the base grid is unstructured, the GCI still applies as long as a systematic method of grid refinement is used, e.g., refining each base grid cell into four new cells gives $r = 2$. However, if the refinement is also unstructured, as occurs when refining the grid only partially in critical areas, a grid refinement index like r to use in Eq.(E.1) must be defined as follows in terms of the total number of elements used in the coarse (N_2) and fine (N_1) grids.

$$\text{effective } r = N1/N2. \tag{E.6}$$

Refinement Procedure

Engineering experience and studies on related problems have led to a grid selection for the base grid so that we are likely in the asymptotic range towards the exact solution. Fining the grid will certainly involve getting more accurate solutions but the computational cost will be unfordable and so infeasible.

Firstly, the hexahedral background mesh has been refined. Note that S_x and B_x for the new mesh must be $\sqrt[3]{2}$ times the same for the previous mesh so as to keep a grid refinement index close to 2. (See Figure 5.2 to review some design parameters shown in the table below).

MD	S_x	S_y	S_z	B_x	B_y	B_z	GP	C_m	C_t	CC	GCI
#1	15	72	18	4	10	10	97287	0.106	0.847		
#2	20	96	24	4	10	10	191858	0.105	0.829	1.32	0.0217
#3	30	144	36	4	10	10	389145	0.103	0.813	1.35	0.0196
#4	30	144	36	5	13	13	422265	0.103	0.812	1.07	0.0012
#5	30	144	36	6	16	16	448145	0.103	0.812	1.09	0.0000
MD	RL1a	RL1b	RL2a	RL2b	RL3a	RL3b	GP	C_m	C_t	CC	GCI
#6	0	1	1	2	1	2	199522	0.105	0.829		
#7	1	1	2	2	2	2	357244	0.104	0.818	1.07	0.013
#8	1	2	2	3	2	3	627228	0.103	0.811	1.41	0.008
#9	1	2	3	4	3	4	1345019	0.103	0.807	1.65	0.005

Table E.1: Refinement study. MD: Mesh Design, GP: Grid Points, CC: Computational Cost defined as n times the previous, GCI: Grid Convergence Index.

where RL1a and RL1b correspond to the surface refinement level for the gullet and drive shaft surfaces with less and more curvature respectively, RL2 is associated to the impeller region and RL3 to the stator, vanes and rear outlet.

The first study for S_x and B_x has been carried out maintaining the refinement levels for `snappyhexmesh` to a minimum. Secondly, mesh resolution adjustments have been made to the second mesh design (#2) in order to refine the computational grid in critical zones and evaluating the influence of each part of the mesh on the final result.

Glossary

Blade back Negative pressure side of the blade facing the front of the pump.

Blade face Positive pressure side of the blade facing the rear of the pump.

Blade root Part of the blade attached to the hub.

Blade tip Part of the blade that is on the outer edge nearest the shroud or jet-pump housing.

Cavitation Phenomena in which the separation or implosion of air and water and the associated heat occurs creating cavities of air and so damaging the impeller, pump and performance of the craft.

Drive shaft Torque is transfered to the impeller from the engine via this shaft.

Gullet Intake housing which channels water toward the impeller.

Hub Center of the impeller which fits over the drive shaft.

Impeller Propeller which resides within a pump housing in a PWC. It is known as propeller when unshrouded not placed within a duct.

Kick Area that is nearest the trailing edge of the impeller blade and adds more pitch relative to its initial value at the leading edge.

Leading Edge (LE) Part of the impeller nearest the front of the pump.

Leading Edge Root Part of the leading edge nearest the hub.

Leading Edge Tip Part of the leading edge nearest the shroud.

Pitch Blade angle measured throughout the outside diameter of each blade or blade tip.

Rake Angle of the impeller blade in correspondence to the hub.

Stators Vanes located immediately after the trailing edge of the impeller that re-direct spiraling or swirling flow into a straighter trajectory .

Sweep Angle of the leading edge in relation to the hub perpendicular where the first attaches the hub..

Trailing Edge (TE) Part of the impeller nearest the rear of the pump.

Trailing Edge Root Part of the trailing edge nearest hub.

Trailing Edge Tip Part of the trailing edge nearest the shroud.

Venturi Shroud right after the jet pump housing that accelerates water.

References

J. Allison. Marine waterjet propulsion. *SNAME*, 101:275–335, 1993.

Bombardier. Seadoo shop manual, bombardier recreational products. 1, 1999.

J. Bredberg. On the wall boundary condition for turbulence models. 2000.

N.W.H. Bulten. Numerical analysis of a waterjet propulsion system. 2006.

CAESES. Official web site, url: https://www.caeses.com. 2017.

E. Dick. Fundamentals of turbomachines. *Springer*, 2015.

S.L. Dixon and C.A. Hall. Fluid mechanics and thermodynamics of turbomachinery, 5th. 1998.

J.H. Ferziger and M. Perić. Computational methods for fluids dynamics. *Springer*, 2002.

The OpenFOAM Foundation. Openfoam user guide, version 4.0. 2016.

G. Hauke. An introduction to fluid mechanics and transport phenomena. *Springer*, 2008.

H. Jasak. Error analysis and estimation for the finite volume method with applications to fluid flows, 1996.

A. Kelth, C. Hamish, and T. Terwisga. Waterjet-hull interaction: Recent experimental results. *SNAME*, 102:87–105, 1994.

T. Maric, J. Hopken, and K. Mooney. The openfoam technology primer. *Sourceflux*, 2014.

F. Moukalled, L. Mangani, and M. Darwish. The finite volume method in computational fluid dynamics, an advanced introduction with openfoam and matlab. *Springer*, 2015.

W. Park, J. Jang, H. Chun, and M. Chan Kim. Numerical flow and performance analysis of waterjet propulsion system. *ScienceDirect*, 2005a.

W. Park, J. Jang, H. Chun, and M. Chan Kim. Numerical flow simulation of flush type intake duct of waterjet. *ScienceDirect*, 2005b.

H. Peixin and Z. Mehrdad. Investigations of 3d turbulent flow inside and around a waterjet intake duct under different operating conditions. *Journal of Fluids Engineering*, 1999.

P.J. Roache. A method for uniform reporting of grid refinement studies. *Journal of Fluids Engineering*, 116/413, 1994.

H. K. Versteeg and W. Malalasekera. An introduction to computational fluid dynamics. the finite volume method. 1995.

WARTSILA. Water-jet propulsion systems official dealer wartsila, url: https://www.wartsila.com. 2017.